

THE UNIVERSITY OF CALGARY

Texture Estimation and Texture Classification
of the SAR Image of Sea Ice

by

Jin Huang

A THESIS

SUBMITTED TO THE FACULTY OF GRADUATE STUDIES
IN PARTIAL FULFILLMENT OF THE REQUIREMENTS FOR THE
DEGREE OF MASTER OF SCIENCE

DEPARTMENT OF GEOMATICS ENGINEERING

CALGARY, ALBERTA

SEPTEMBER, 1996

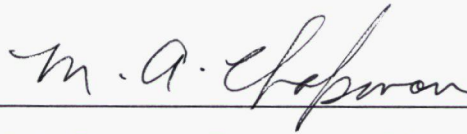
© Jin Huang 1996

THE UNIVERSITY OF CALGARY
FACULTY OF GRADUATE STUDIES

The undersigned certify that they have read, and recommend to the Faculty of Graduate Studies for acceptance, a thesis entitled "Texture Estimation and Texture Classification of the SAR Image of Sea Ice" submitted by Jin Huang in partial fulfillment of the requirements for the degree of Master of Science.



Supervisor, Dr. M. J. Collins, Department of Geomatics Engineering



Dr. M. A. Chapman, Department of Geomatics Engineering



Dr. B. R. Petersen, Department of Electrical and Computer
Engineering

Sept. 30, 1996

Date

ABSTRACT

Synthetic Aperture Radar image texture remains an untapped source of information about the imaged scene. The objective of texture analysis is to characterize and discriminate between environmental scenes based on the expression of the texture in the SAR image data. In our research, the autocorrelation function (ACF) is used to describe the image texture. We have developed a simple one-dimension ACF model which includes the focus error.

We have chosen sea ice as the environmental scene. We studied the effect of the system parameter on the estimation of SAR image texture and tested the ability of the ACF model to discriminate three ice types: undeformed new ice, deformed new ice and first year/brash ice matrix. The results indicate that the system parameter has a key role in the performance of the ACF. Texture classification based on the ACF parameter estimation is found to be feasible.

ACKNOWLEDGMENTS

I am very grateful to my supervisor, Professor M. J. Collins for his kind instruction and encouragement throughout my research program. Thanks are given to Liming Qian and Liming Wu for their technical help with computer. I also thank Christine Pelletier and Derek Lichti for proofreading.

I gratefully acknowledge the Teaching and Graduate Research Assistantships from the Department of Geomatics Engineering.

The research was supported by a NSERC (National Science and Engineering Research Council of Canada) grant to Professor M. J. Collins

To my parents
for their enduring guidance and moral support
throughout my life

TABLE OF CONTENTS

Approval Page.....	ii
Abstract	iii
Acknowledgments	iv
Dedication	v
Table of Contents	vi
List of Tables	ix
List of Figures	xi
CHAPTER 1 INTRODUCTION	1
1.1 Motivation of the Study	1
1.1.1 SAR Image Texture Analysis	1
1.1.2 Sea Ice	2
1.2 Research Objective	4
1.3 Thesis Outline	7
CHAPTER 2 THE SAR IMAGING SYSTEM	9
2.1 Introduction	9
2.2 Geometry of Imaging Radar	10
2.3 Radar Image Processing	13
2.3.1 Matched Filter Receiving	13
2.3.2 Synthetic Aperture Radar	15
2.4 A Model for the SAR Imaging System	18
2.5 Autofocus Technique	21
CHAPTER 3 STATISTICAL ANALYSIS OF YOUNG ICE IN THE LABRADOR SEA MIZ	23
3.1 Formation and Physical Properties of the Sea Ice	23
3.2 Statistical Model of Young Ice	24

3.2.1 Backscattering Model	25
3.2.2 Spatial ACF of the Image	28
3.2.3 Second-order Single Moment Model	33
3.3 Texture Classification	34
3.3.1 Texture Classification Based on the ACF Model	35
3.3.2 Parameter Estimation Accuracy	36
CHAPTER 4 EXPERIMENTAL PROCEDURE AND DATA	39
4.1 Experiment design	39
4.2 Experimental Data Acquirement	40
4.2.1 SAR System	42
4.2.2 Aerial Photography	42
4.3 Studied Scene	43
4.3.1 Target A: Undeformed New Ice	43
4.3.2 Target B: Deformed New Ice	43
4.3.3 Target C: Large First Year/Brash Ice Matrix	44
CHAPTER 5 RESULTS AND DISCUSSION	50
5.1 Nonlinear Model Fitting Method	50
5.2 Comparison of the Two ACF Models	52
5.3 The Effect of Processed Bandwith on the ACF Model	54
5.4 The Effect of Processed Bandwith on the Parameters of the ACF Model	54
5.4.1 The Effect Of Processed Bandwidth on the System Resolution	54
5.4.2 The Effect Of Processed Bandwidth on the Order Parameter.....	54
5.4.3 The Effect Of Processed Bandwidth on the Correlation Length	55
5.5 The Standard Deviation of the Estimated Parameters	56
5.6 Second-order Single Moment	56
5.7 Texture Classification of the Sea Ice	65
5.7.1 Estimated Parameters of the Three Ice Types	65
5.7.2 Fractional Error of the Estimated Value	66
5.7.3 Texture Parameters of the Subimage	67

CHAPTER 6 CONCLUSIONS AND RECOMMENDATIONS 80
 6.1 Conclusions 80
 6.2 Recommendations 81

REFERENCES 82

LIST OF TABLES

Table 3.1	A summary of conditions for K-distributed target and their physical meaning	28
Table 3.2	The simulation values of the texture parameters corresponding to the classes	38
Table 4.1	The main technical specifications for the CCRS IRIS in high resolution mode	45
Table 5.1	Merit function χ^2 of targets A and Target C with trial focus error $\eta'=0.00$. The first row of each processed bandwidth n represents the results of the ACF model concerning the focus error in which the system resolution is estimated by fitting the ACF model to the measured ACF. The second row of each n represents the results of the ACF model not concerning the focus error in which the system resolution is fixed assuming the image is perfectly focused.....	58
Table 5.2	The system resolution at different processed bandwidths n for each channel of targets A and C with the trial focus error $\eta'=0.00$. The system resolution is estimated by fitting the ACF model to the measured ACF.....	59
Table 5.3	The order parameter at different processed bandwidths n for each channel of targets A and C with the trial focus error $\eta'=0.00$. The order parameter is estimated by fitting the ACF model to the measured ACF.....	60
Table 5.4	The correlation length at different processed bandwidths n for each channel of targets A and C with the trial focus error $\eta'=0.00$. The correlation length is estimated by fitting the ACF model to the measured ACF.....	61
Table 5.5	The standard deviation of the order parameter at different processed bandwidths n for each channel of targets A and C with the trial focus error $\eta'=0.00$. The standard deviation of the order parameter was the output of the Levenberg-Marquardt routine when the ACF model was fit to the measured ACF	62
Table 5.6	The standard deviation of correlation length at different processed bandwidths n for each channel of targets A and C with the trial focus error $\eta'=0.00$. The	

standard deviation of correlation length was the output of the Levenberg-Marquardt routine when the ACF model was fit to the measured ACF ... 63

Table 5.7	The second-order single moment at different processed bandwidths n for each channel of targets A and C with the trial focus error $\eta'=0.00$. These results are mean values of the measured second-order single moment in the azimuth direction	64
Table 5.8	The texture parameters of γ and x_0 and their standard deviation, azimuth length: 1024, $n=1$ with the trial focus error $\eta'=0.00$	69
Table 5.9	The theoretical prediction and experimental result of the fractional error for targets A, B and C. The azimuth size of the target area is 1024, $n=1$, the trial focus error $\eta'=0.00$	70

LIST OF FIGURES

Figure 2.1	Radar geometry with the transmitted pulse and its resulting footprint	11
Figure 2.2	Spherical propagation wavefront of the transmitted and scattered field	15
Figure 2.3	Geometry in SAR	17
Figure 3.1	Large regions of textures with varying correlation lengths (rows) and order parameters (columns)	38
Figure 4.1	Location of LIMEX experimental sites	41
Figure 4.2	The overview of the location of the studied area. This is CCRS CHH SAR image data. The Target F in the image is named Target C in this thesis . . .	46
Figure 4.3	Target A: Undeformed new ice	47
Figure 4.4	Target B: Deformed new ice	48
Figure 4.5	Target C: Large first year/brash ice matrix	49
Figure 5.1	Measured and modeled ACF. Target A, Channel CHH, $n=1$, the trial focus error $\eta'=0.00$. The solid line represents the measured ACF; the dashed line represents the modeled ACF with focus error; the circles represent the ACF model not considering the focus error	71
Figure 5.2	Measured and modeled ACF. Target A, Channel XHV, $n=1$, the trial focus error $\eta'=0.00$. The solid line represents the measured ACF; the dashed line represents the modeled ACF with focus error; the circles represent the ACF model not considering the focus error.	72
Figure 5.3	Measured and modeled ACF. Target A, Channel CHH, $n=1$, the trial focus error $\eta'=0.05$. The solid line represents the measured ACF; the dashed line represents the modeled ACF with focus error; the circles represent the ACF model not considering the focus error	73
Figure 5.4	Measured and modeled ACF with different n . Target F, Channel CHH, the trial focus error $\eta'=0.03$. The solid line represents the measured ACF; the	

dashed line represents the modeled ACF with focus error; the dotted line represent the ACF model not considering the focus error 74

Figure 5.5 Modeled ACF of Target A of different channels, the trial focus error $\eta'=0.02$. The solid line represents the modeled ACF with focus error. The dashed line represents the ACF model not considering the focus error 75

Figure 5.6 The histogram of γ of subimages (azimuth length: 128), channel XHH, $n=1$, the trial focus error $\eta'=0.00$ 76

Figure 5.7 The histogram of γ of subimages (azimuth length: 128), channel CHV, $n=1$, the trial focus error $\eta'=0.00$ 77

Figure 5.8 The histogram of x_0 of subimages (azimuth length: 128), channel CHH, $n=1$, the trial focus error $\eta'=0.00$ 78

Figure 5.9 The histogram of γ of subimages (azimuth length: 128), channel CHH, $n=1$, the trial focus error $\eta'=0.00$ 79

CHAPTER 1

INTRODUCTION

This chapter first outlines of the motivation for the texture analysis of the Synthetic Aperture Radar (SAR) image of sea ice in marginal ice zone. Then it describes the specific objective of the research and the tools used in texture analysis. The autocorrelation function (ACF) is chosen to describe the image texture in this research. The last part of this chapter introduces an outline of the thesis.

1.1 Motivation for the Study

1.1.1 SAR Image Texture Analysis

Synthetic Aperture Radar (SAR) is an important technology with several advantages, including (1) day/night and all weather imaging, (2) geometric resolution independent of sensor altitude or wavelength, and (3) signal data characteristics unique to the microwave region of the electromagnetic (EM) spectrum (Curlander and McDonough, 1991). The platform used in SAR systems can be an aircraft or a satellite. The image acquisition is very fast and the image scale is large. For example, a high resolution SAR system can achieve a resolution of about 0.3m by 0.3m (Posner, 1993). These advantages have led to widespread usage of SAR imaging systems in civilian remote sensing besides its usage for military applications.

Among all the remote sensing sensors, SAR is relatively new. Consequently, SAR image texture remains an untapped source of information about the imaged scene. Texture analysis is an important aspect in scene analysis because texture is a special kind of characteristic of picture regions which corresponds to the physical surface (Chen, 1980). Texture of an image represents the frequency of tonal change on an image. In another words, a texture is composed of primitives arranged in terms of a specific relationship; the primitive is a collection of pixels in which each one shares a common tonal property and is geometrically connected. These primitives are related to the texture according to a spatial relationship which may be probabilistic, structural or both in nature. The word “scene” is used to refer to all scatterers from the same class.

The objective of texture analysis is to characterize and discriminate between environmental scenes based on the expression of the spatial backscatter fluctuations, or texture, in the SAR image data.

For distributed scenes, there are many small individual reflectors within a given pixel. The individual reflectors might be deployed spatially in such a way as to cause destructive or constructive interference in the sum of their reflectance. Some pixels would therefore appear unnaturally bright or dim. This “salt and pepper” texture is called speckle. The image texture is thus a mixture of speckle and target texture.

1.1.2 Sea Ice

Sea ice has important consequences to human activity. Sea ice has an intimate and complex role in the ocean-ice-atmosphere system. In this system, there are thermal and

mechanical energy transfers over a large spatial and temporal range. The key factor controlling surface energy fluxes and the available net radiation is the high albedo of the ice and snow covered surface (Barry, 1983). There are significant turbulent heat fluxes from the oceans to the atmosphere through leads (cracks in the ice), young, thin ice (up to one metre thick) in winter because of their relatively small albedo in winter. This leads to a large heat transfer. Therefore, the young ice has a significant roll in the winter energy budget. It is estimated that half of the heat flux over a year occurs through 20-80 cm thin and young ice, whose area is only about 6 percent of the ocean in winter (Maykut, 1978).

The distribution of the sea ice and the atmosphere are fully coupled in the dynamic ocean-ice-atmosphere system (Herman, 1986). The change of the sea ice will affect the heat fluxes, which may bring a positive feed back to the atmosphere activity, for example, storm. Herman and Johnson (1978) predicted in their experiment that the raising of the sea level as a result of the melting of the sea ice which is the effect of the temperature raising of the earth would increase precipitation over northern Europe.

Sea ice also greatly affects maritime activity, such as navigation and offshore oil and gas drilling. The mechanical action of ice on offshore structures is probably the most important environmental factor affecting the design of these offshore structures. The mechanical characteristics, such as compressive strength, tensile strength, shear strength and flexural strength, are determined by the type of ice. Each different type of ice has a different crystal structure and a different age. When designing the drilling platform, the sea ice types around the oil and gas reserve must first be determined. Sea ice is also a significant hazard to shipping. The path of the ship should be through the young and thin

ice areas for the reason of safety. Based on all of these needs, acquisition of the sea ice distribution is essential.

Most offshore activity occurs in what is called the marginal ice zone (MIZ). MIZ may be defined as “an ice cover which is close enough to the open ocean to be affected by its presence” (Wadhams, 1986). The multiplicity in size, shape and type of the ice characterize this zone. The MIZ of great commercial value to Canada is in the Labrador Sea and extends from Baffin Bay to the Grand Banks (Collins, 1993). A large international field experiment known as LIMEX (Labrador Ice Margin Experiment) (Carsey, Argus, Collins, Holt, Livingstone and Tang, 1989) took place at this site in the spring of 1989. The SAR data used in this study is from this experiment. The ice in this zone is predominantly first year ice with 0.01%-8% multiyear ice (Zakrzewski, 1986).

1.2 Research Objective

The traditional way of getting the spatial distribution of sea ice types is from the records from isolated ships and stations which are unfortunately sparse. The cost and hazards of these observations are large, and the time and spatial scale for which information is acquired cannot meet our needs. Consequently, remote sensing is especially suitable for this large spatial scale data acquisition of sea ice because of its time and cost savings characteristics. Imaging radar, one of the sensors in remote sensing, has been shown to be the most effective tool for acquiring regional sea ice information on an operational basis (Falkingham, 1991). Due to its high resolution, the SAR, one of the radar imaging system, was used in LIMEX because of its high resolution.

SAR is an active imaging system using coherent electromagnetic radiation. Like all coherent imaging systems, such as the laser, the image from SAR is degraded by speckle. The speckle cannot be considered as noise. It also carries some information of the scene texture. Thus the SAR image used in this research is not speckle deducted.

My objective in the study is to perform sea ice classification based on the texture difference of different types of sea ice. Mathematical models are very important and useful in the development of image processing algorithms. Although, it is possible to develop heuristic algorithms for some of the easier image processing tasks, model based procedures are necessary for developing optimal algorithms for more difficult image processing problems. The optical imaging system can be modeled as a linear system with additive Gaussian noise. However, the imaging process of the radar is significantly different than the optical systems due to the coherent nature of the illumination.

The linear additive Gaussian noise models cannot be applied to the radar imaging systems. The image processing algorithms, which are based on additive Gaussian noise models, would fail when they are used on radar images. The models for radar image processing were developed with consideration of the local and global statistical properties of radar images (Frost, 1982).

In many texture applications, such as texture classification, texture edge detection and image segmentation etc., the success of the algorithm is highly dependent upon the selection of the texture properties (Davis, 1975). There are many ways to describe texture:

- Cooccurrence matrix. This matrix is an estimation of the second order statistics of the image $P(\delta x, \delta y, i, j)$. $P(\delta x, \delta y, i, j)$ is the probability that two pixels of distances δx and δy in x and y directions have intensity i and j . Generally, the cooccurrence matrix can provide a powerful texture discrimination capability. But it cannot fully identify every texture (Chen, 1980).
- Statistical mean estimator and variance estimator. This method assumes the image is a two-dimensional discrete random field and the random variables in the field are stochastically independent. The assumption implies that the ensemble statistics are the same as the spatial statistics. This is not a realistic model because in most images, the pixels are spatially correlated.
- Means and the covariance matrix of the intensity of the pixels in the image.
- The Fourier Power Spectrum (FPS). This power spectrum reflects the distribution of the coarseness of the texture. This spectrum is biased if the image is directionally-biased. Another problem is the difficulty of evaluating the spectrum over non-square regions (Palidis, 1977).
- Gray level run length (Galloway, 1975). In this approach, the texture description is contained in the four intensity level run length matrices. Each matrix is evaluated for each of the four directions. This method is quite good for the linearly-structured texture.
- Autocorrelation function (ACF) (Rosenfeld and Weszka, 1976). The first order statistics (PDF) cannot reflect the correlation in the image pixel. Thus the second

order statistic (ACF) is necessary to give more complete description of the image. C. J. Oliver has made significant contribution to SAR image texture analysis using ACF.

In our research, the ACF was used to describe the natural clutter texture in the high-resolution SAR image. Clutter is defined as a collection of randomly distributed elemental scatterers with no scatterer dominating (Posner, 1993). The ACF model was based on a statistical model of the field and a simplified imaging function.

The purpose for which we constructed an ACF model to represent the backscatter's two-point statistics was to estimate backscatter texture parameters from SAR image using the ACF as a texture description tool. The parameters estimated through the ACF model reflect the texture's characteristics and can be used to perform image classification. However, the discrimination power of the ACF texture parameters is significantly weakened by a large ACF variance. A key issue in this approach is the accuracy with which we can estimate the ACF model parameters.

1.3 Thesis Outline

Chapter 2 gives a brief description of the SAR imaging system. SAR is different from the traditional real aperture image radar. Through its synthetic aperture, SAR gains high along-track resolution. The SAR imaging system consists of 2 parts: (1) collection of a sampled target diffraction pattern and (2) reconstruction of the target backscatter field through range and azimuth matched filtering.

The spatial statistics of the sea ice is studied in Chapter 3. Based on the analysis, models of the ACF and second-order single moment (the square of the reflected intensity from the scene), are constructed. Texture classification is performed by using the estimated parameters of the ACF model. The estimation accuracy of these parameters in ACF is essential to show the classification reliability.

Chapter 4 describes the data source and the experiments designed to test the models we built and the classification ability of the ice texture parameters.

Chapter 5 shows the results of the experiments designed in Chapter 4. The interpretation of the results is also in this chapter.

Discussions and recommendations are given in Chapter 6.

Information extraction from radar images will continue to be an important and interesting area of study. The extraction of the texture information of the target was addressed in this work. The models derived here will provide one method of extracting and analyzing the information contained in SAR images.

CHAPTER 2

THE SAR IMAGING SYSTEM

This chapter reviews the SAR imaging system. First, it presents a brief history of SAR. Then it describes how SAR works and the signal processing method. A model for SAR imaging system is constructed based on these system description. Finally the autofocus technique is reviewed.

2.1 Introduction

SAR is an active remote sensing system. The radar transmits an electromagnetic wave towards the ground target area and records the reflected wave. The characteristics of the reflected wave, for example, amplitude, phase and polarization, etc., primarily depend on three reflecting surface parameters: (1) dielectric constant; (2) roughness (rms height); and (3) local slope. Imaging radar records the reflected wave and the corresponding time delay to determine the object characteristics and the relative position of the object.

Before the discovery of synthetic aperture radar in the early 1950's, radar had long been used as a tool for detecting and tracking metallic targets such as aircraft and ships. In the early 1950's, it was found that the radar could be fixed to the fuselage of the aircraft instead of rotating the antenna to scan the target area. This is the early version of imaging radar called side-looking real-aperture radar (SLAR). The value of SLAR images for scientific applications such as geologic mapping, oceanography and land use studies

was recognized almost immediately (McDonald, 1969). Based on SLAR, SAR was designed by Carl Wiley of Goodyear Aircraft Corp. in June 1951 (wiley, 1985). In 1953, the first airborne high resolution SAR system was built by the radar group at the Goodyear research facility in Litchfield, Arizona (Curlander and McDonough, 1991). It is the image resolution in the dimension parallel to the direction of flight (i.e., the azimuth or along-track dimension) that distinguishes a SAR from other imaging radar systems. To achieve high resolution in the azimuth dimension, SAR uses a coherent system to record the amplitude and phase information of the echo. Now, SAR is widely used in remote sensing. After the airborne SAR systems, there are spaceborne SAR systems. In 1972, the Apollo Lunar Sounder Experiment was performed. In this experiment, Apollo 17 carried a coherent SAR system to map the lunar surface at radar wavelengths. The success of this experiment led NASA in 1975 to approve a SAR as one of the remote sensors on Seasat. The scientific results from Seasat quickly led to the approval by NASA of the series of flights of the Shuttle Imaging Radar (SIR).

2.2 Geometry of Imaging Radar

In the imaging radar system, the transmitting antenna sends out the electromagnetic wave for the duration T . Then the transmitting antenna is shut off. This signal is called a pulse of duration T . The pulse emitted from the antenna will illuminate some target area. For radar systems which are scanning the earth's surface, the area illuminated by one pulse is called the radar's footprint (Fitch, 1988). Swath is defined as

the strip covered by the footprint when the radar moves forward. Figure 2.1 shows the geometry with the transmitted pulse and its resulting footprint.

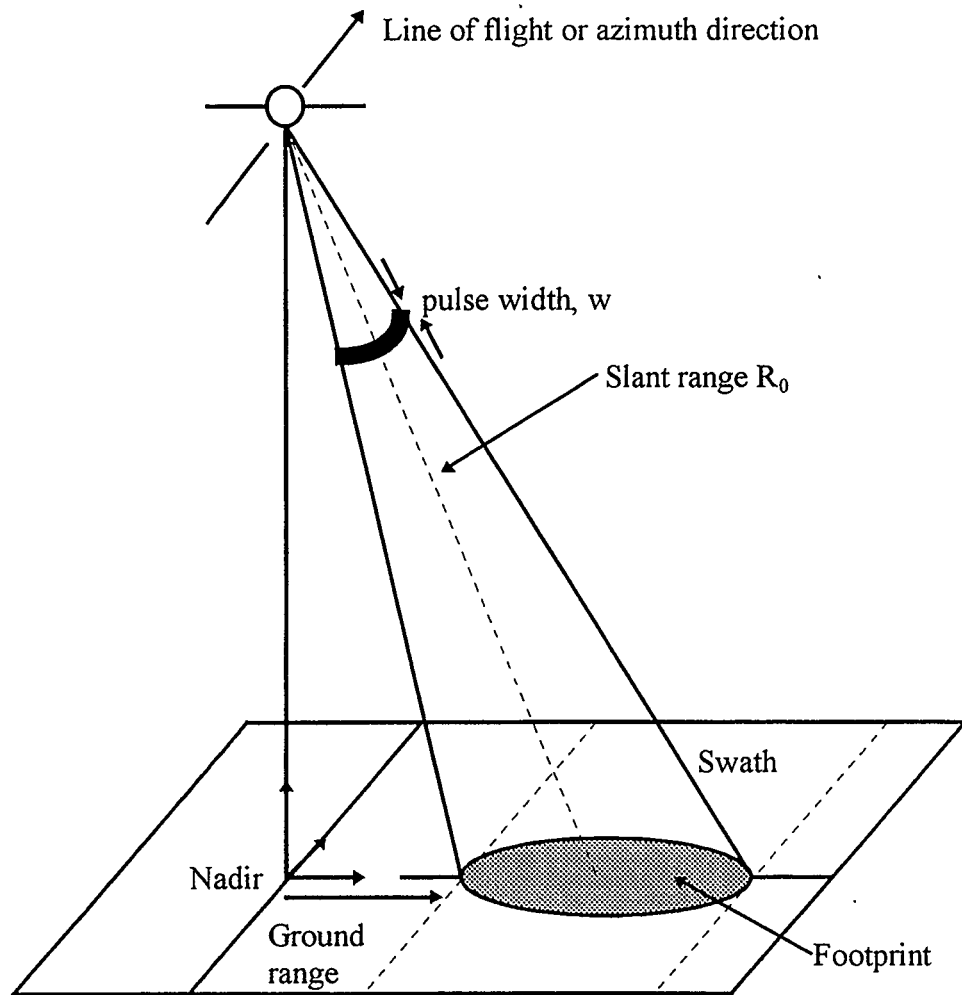


Figure 2.1 Radar geometry with the transmitted pulse and its resulting footprint.

The flight direction of the aircraft is called the azimuth direction. Ground range and slant range are shown in Figure 2.1. We assume that the transmitting antenna is turned on for a very short time, and then off again, which means that T is very small. Therefore, a brief burst of radio energy is emitted, which is pictured as a shaded band of width w in Figure 2.1. If the two reflectors in the footprint are closer together than the width w of the pulse, the two targets would blur together so that they could not be separate them in the image.

The size of the footprint is determined by the antenna beam width. The transmitting/receiving antennae are characterized by a three dimensional gain pattern which has fading side lobes. In this study, only the center lobe is modeled and the sidelobe effect is ignored as most of the energy transmitted by the antenna is in the center lobe. Thus, the radar system antenna pattern can be modeled as a Gaussian function for simplicity.

The SAR system uses a digital computer to process the raw data into an image. After one pulse is sent out at a certain azimuth position, the receiver will sample the reflected signal. This implies that one continuous echo will generate an entire row of discrete data points. The sampling rate should obey the Nyquist sampling principle to keep the resolution in the range dimension. After the echo is sampled, one strip of signal is obtained. The width of this strip in the azimuthal direction is equal to the azimuth beamwidth on the ground. By turning the transmitter on and off, many strips are obtained as the airplane moves forward. These strips thus form a two-dimensional image. The

pulse rate should also obey the Nyquist sampling principle which relates to the azimuth resolution.

2.3 Radar Image Processing

SAR systems are designed and operated to be linear in the various voltage waveforms (Curlander and McDonough, 1991). In the SAR system, the operation of average power formation at the IF (Intermediate Frequency) output is replaced with the linear operation of “quadrature demodulation”, also called “I, Q detection”. In this, the high frequency structure of the IF signal is shifted to a frequency band centered on zero frequency, leaving the low frequency envelope waveform (Whalen, 1971).

2.3.1 Matched Filter Receiving

The noise due to interfering radiation, atmospheric and thermal effects degrades the ideal transmission and reception of the radar signals. The overlap of the returning radar pulse from closely spaced objects causes signal ambiguity. Thus the effective duration and energy of the transmitted pulse determine the resolution and maximum range, respectively, of a radar system. Shorter duration pulses allow closely spaced targets to be discriminated, while high energy pulses provide measurable reflections from targets at large ranges. However, it is difficult and expensive to develop the hardware to generate a short pulse with large energy. The autocorrelation of the received signal can compress the pulse and remove part of the noise. Therefore, this technique is used in SAR signal range and azimuth compression (Cenzo, 1981. Fitch, 1988. Curlander and McDonough, 1991).

A linear or nonlinear Frequency Modulation (FM) (chirp) format is often used for pulse coding while a correlation receiver is used for compression (Fitch, 1988). The correlation receiver is also called a matched filter. The maximum range resolution of the image is determined by the bandwidth of the transmitted pulse. Let $u(t)$ be the transmitted signal and $r(t)$ be the received signal and let $r(t)$ be a time delay of $u(t)$. Thus, the received signal can be written as:

$$r(t) = \sigma u(t-\tau) \quad (2.1)$$

where σ is cross section of the reflector and τ is the two-way travel time.

The output of the matched filter is:

$$y(t) = \int u^*(s)r(s+t)ds = \sigma \int u^*(s)u(s+t-\tau)ds \quad (2.2)$$

where $*$ denotes complex conjugate relationship.

The linearity of the correlation operation implies that this receiver can be expressed as the convolution of the received signal with the impulse response $h(t)$. Thus Equation (2.2) can be written as:

$$y(t) = \int u^*(s)r(s+t)ds = \int r(s)u^*(-(t-s))ds = \int r(s)h(t-s)ds \quad (2.3)$$

where,

$$h(t) = u^*(-t) \quad (2.4)$$

A stable local oscillator (STALO) is usually required to produce a reference signal to mix with the echo so as to keep the phase information contained in a radar echo. This is called coherent receiving.

2.3.2 Synthetic Aperture Radar

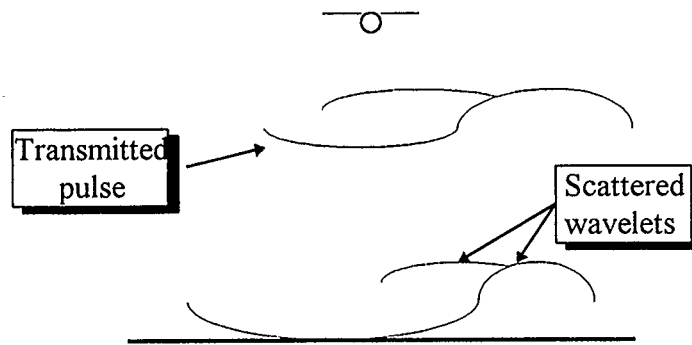


Figure 2.2 Spherical propagation wavefront of the transmitted and scattered field.

For real aperture radar the resolution in the azimuth direction depends on the physical length of antenna in this direction. The longer the antenna, the smaller the resolution. Hence, a very long antenna is needed to achieve high along-track resolution. For example, to achieve a 25m resolution in azimuth in Seasat, the antenna should be over 8km (Fitch, 1988). It is not feasible for either satellites or aircraft to carry antennae more than 1km long. However, an antenna array made up of antennae of small size can achieve the same result. The wavefront of the echo has a spherical shape (see Figure 2.2). Thus,

for a linearly placed antenna array of which the antennae are placed along a straight line, the sum of the signal from different subapertures is performed after a certain delay for each subaperture. The length of the antenna array is the real aperture of the radar system. The number of positions required to sample the antenna array for an arbitrary input are specified by Nyquist's theory applied to the spatial bandwidth of the collected signal in the azimuth direction.

Because of the weight and size restriction of the platform, the larger aperture antenna array does not physically exist in SAR. A single and physically small antenna is used to collect the data. The larger aperture is synthesized by sequentially gathering at different positions which collectively define the antenna array. The solution is known as Synthetic Aperture Radar (SAR).

Figure 2.3 shows the geometry in SAR. β is defined as the beam width in the azimuth direction. X is the width of the power envelope of the physical antenna corresponding to the azimuth width of radar footprint, which is known as the synthetic aperture in SAR literature. For high resolution SAR systems, β is quite small. Therefore, the X can be written as:

$$X = R_0\beta \quad (2.5)$$

where R_0 is the slant range of the footprint center.

The spatial bandwidth of the recorded data is given by:

$$B = \frac{2\beta}{\lambda} \quad (2.6)$$

where λ is the wavelength.

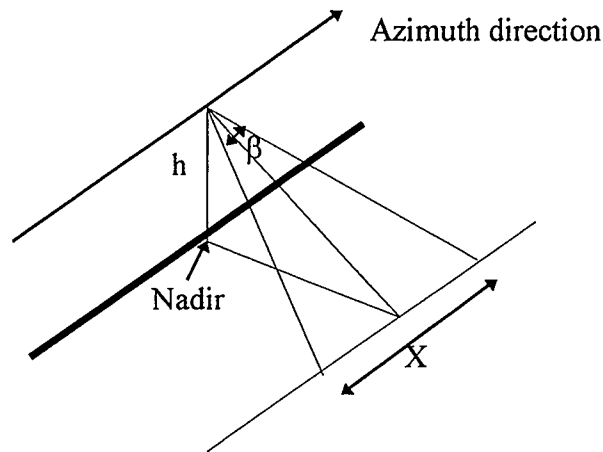


Figure 2.3 Geometry in SAR

An unfocused array can be synthesized by averaging echo signals at some fixed time delay bin over a window in the azimuth direction. Due to the fact that the wavefront of the echo has a spherical shape, the resolution is degraded by the curved wavelet effect which is called range migration of the target echo. The range migration is coupled with the range and azimuth coordinates. The focused SAR is achieved by averaging the echo along a hyperbolic line in the azimuth direction. Each output range requires a particular shift of the surrounding data to create the focusing effect.

The range dependent delay and summation operation for focusing a synthetic aperture can be described by a matched filter similar to the pulse compression procedure

described in Section 2.1. The pulse compression of the range echo is committed before focusing the synthetic. The azimuth phase term provides the shape for the reference function.

2.4 A Model for the SAR Imaging System

This study was only concerned with the azimuth direction of the SAR image. Therefore, a one-dimensional system model was adopted. Synthetic aperture radar is a coherent imaging system which consists of two parts: (1) collection of the target diffraction pattern and (2) reconstruction of the target image through matched filter processing (Collins, 1993). M. J. Collins built a model of the imaging system based on this description and this model was used in this research.

From Section 2.3.2 it is known that when we reconstruct the synthetic aperture in the azimuth direction, due to range migration, the data should have an appropriate delay before being summed. Since the data used in this study was collected by the airborne SAR system, the effect of range migration was neglected. This model also neglects the effects related to target motion and used a Gaussian function to model the center lobe of the antenna pattern. Thus, the diffraction pattern of the signal can be simply represented by a diffraction filter h_d (Goodman, 1968; Collins, 1993):

$$h_d(x) = \exp\left\{-\pi \frac{x^2}{X^2}\right\} \exp\left\{-j\pi \frac{x^2}{\chi_0^2}\right\} \quad (2.7)$$

where x is the spatial azimuth coordinate. X is the synthetic aperture defined in Section 2.3.2. It is equivalent to the width of the available diffraction pattern. The width of the quadratic phase term χ_0 is written as:

$$\chi_0 = \frac{X}{B} = \sqrt{\frac{R\lambda}{2}} \quad (2.8)$$

where the spatial bandwidth, B , is defined in Section 2.3.2.

After the diffracted wave is collected by the receiver, a matched filter is needed to reconstruct the image. This matched filter may also select an arbitrary segment or look of the recorded signal with a real Gaussian weighting function. According to Equations 2.4 and 2.7, the matched filter may be written as:

$$h_m(x) = \exp\left\{-\pi \frac{x^2}{X^2}\right\} \exp\left\{j\pi \frac{x^2}{\chi_0^2}\right\} \exp\left\{-\pi \frac{x^2}{X_n^2}\right\} \quad (2.9)$$

where X_n is called the look width which decides the fraction of the available signal selected for processing and can be written as:

$$X_n = X / n \quad (2.10)$$

where $1/n$ is the fraction of the total available aperture.

In the diffraction model, the range migration is neglected. Thus, the matched filter constructed based on this model has a small phase mismatch with the real signal which

results in an imperfectly focused radar system. This is commonly termed as *focus error* in SAR literature. The matched filter model with a focus error is:

$$h_m(x) = \exp\left\{-\pi \frac{x^2}{X^2}\right\} \exp\left\{j\pi \frac{x^2}{\chi^2}\right\} \exp\left\{-\pi \frac{x^2}{X_n^2}\right\} \quad (2.11)$$

where χ is the width of the quadratic phase term with a small fractional focus error η . χ is defined as:

$$\chi = \sqrt{\frac{R\lambda}{2(1+\eta)}} \quad (2.12)$$

The SAR system's complex impulse response of the azimuth channel may be written as:

$$h_c(x) = h_r(x) * h_m(x) \quad (2.13)$$

where “*” denotes the convolution operator. The stationary-phase approximation when performing the Fourier transform and the constant is neglected. The impulse response can be written as:

$$h_c(x) = \exp\left\{-\pi B^2 \frac{K + j\varepsilon}{K^2 + \varepsilon^2} x^2\right\} \quad (2.14)$$

where,

$$K = \frac{1+n^2}{(1+\eta)^2} + 1 \quad \text{and} \quad \varepsilon = XB \frac{\eta}{1+\eta} \quad (2.15)$$

The square law detection of the complex signal yields the image intensity or power. The power response of the image is:

$$h_i = |h_c(x)|^2 = \exp\left\{-2\pi \frac{KB^2}{K^2 + \varepsilon^2} x^2\right\} \quad (2.16)$$

The imaging system resolution which is measured in this study by the equivalent rectangular width (ERW) (Brown, 1963) is:

$$\rho = \rho_0 \sqrt{K + \frac{\varepsilon^2}{K}} \quad (2.17)$$

where ρ_0 is the best achievable resolution which equals $1/B$. The focus error and fractional look width will effect the system resolution according to the model.

2.5 Autofocus Technique

In order to form the SAR image, the incident radiation is convolved with a reference signal. In this research the effect of range migration was neglected. Therefore, there is a mismatch between the echo and the reference. One technique used to correct the mismatch is autofocus (Oliver, 1993). Autofocusing uses post-processing on the SAR images to improve the quality. In this method, the focus parameter is adjusted to maximize the contrast in the compressed pulse. This type of processing does not require

specific knowledge about the scene. It is not dependent on the existence of point targets, as extended targets will also give an autofocusing capability. Indeed, this technique will work provided that there is some variation in the underlying cross-section.

Although autofocusing is used to minimize the mismatch, there is still some uncertainty in the width and sidelobe level of the compressed pulse in a SAR image. In the limit of perfect focusing, the focus error depends not only on the radar trajectory but also on the noise in the received signal. The ideal form of the signal after diffraction, is degraded by a complex Gaussian additive noise component. This noise arises from the interference between random scatterers within the scene. Another source of uncertainty is from the use of a mismatched reference function, arising from uncertainties in the autofocus estimate.

CHAPTER 3

STATISTICAL ANALYSIS OF YOUNG ICE IN THE LABRADOR SEA MIZ

This chapter reviews the physical properties of sea ice. Based on the assumption that the SAR image intensity for sea ice has a K-distribution (Oliver, 1986), the ACF model and second-order single moment model are constructed. This chapter also discusses the possibility of sea ice classification based on the parameter estimation of the ACF model. To measure the classification accuracy, the fractional error in the ACF parameter is introduced.

3.1 Formation and Physical Properties of the Sea Ice

Salts in sea water affect the freezing point approximately according to the equation $T_f = -0.055S_w$ where S_w is the salinity per mil (‰) of sea water (Maykut, 1985). Surface cooling of the sea water produces a density gradient in the upper ocean which yields an unstable vertical density distribution in turn leading to convective mixing until the water reaches freezing point (Weeks and Ackley, 1982). Once the entire mixed layer in the upper ocean reaches freezing point, additional heat loss allows the ice formation to begin.

Sea ice generally contains much less salt than the water from which it freezes. The freezing process rejects most of the salt back to the ocean. As the ice grows, more salt is rejected (Gow and Tucker III, 1991).

Initial ice formation occurs at or near the surface of the sea water in the form of small platelets and needles called *frazil*. Further freezing produces grease ice, a soupy

mixture of sea water and unconsolidated frazil crystals. Under quiescent conditions the frazil crystals quickly freeze together to form a solid, continuous ice cover. However, winds cause turbulence in the water which usually prohibits this solid ice cover formation. Wind and wave action drive frazil crystals downwind and in the sustained wave field, the accumulation of frazil crystals forms pancakes. Finally, the pancakes consolidate by freezing together to form a continuous sheet of ice. This thin sheet of ice would most often deform under compression (Gow and Tucker III, 1991).

Once a continuous ice sheet has formed, ice crystals lose a degree of freedom in their growth. Further ice growth is vertical to the ice sheet. Ice growth causes the important small-scale roughness elements which form many small scatterers. The polycrystalline structure which characterizes the sea ice can occur in several different textures. Differences in crystalline texture and the nature and distribution of brine inclusions are of additional importance in that they exert a major effect on the electrical properties of sea ice and in turn can have a critical bearing on the radar images.

3.2 Statistical Model of Young Ice

The backscatter of the young ice in the Labrador Marginal Ice Zone (MIZ) can be described by a compound scattering model that is the result of two dependent random processes: one governing the variability of an individual pixel, and the other controlling the spatial fluctuation of these per-pixel statistics (Collins, 1993). The young ice in the scale of the SAR resolution may comprise of floes, floe edges, brash ice between the floes,

etc. As with most naturally occurring terrain, sea ice may be regarded as a set of locally homogeneous patches which share some particular set of physical characteristics.

A homogeneous area, such as a field of wheat, has a very narrow correlation function relative to the resolution of the imaging system. Targets like this are called Gaussian and the texture of the image is due to the speckle only. This speckle texture is caused by constructive and destructive interference of the individual reflectors which is not only on a per pixel basis but also on a pixel-by-pixel basis when coherent illumination is reflected from a rough surface. The compound targets, however, involve two components: (1) speckle, (2) texture which is due to the spatial variability in the scattering properties of the scene illuminated by the radar (Posner, 1993). This is often called a non-Gaussian target. Therefore, the statistical character of these scenes can be expressed by two phenomena: one is speckle which is a unit complex Gaussian; the other is the spatially correlated texture. It must be understood that the overall “speckled appearance” of a radar image and the “image texture” in a radar image are both due to the interplay of the two phenomena which are speckle and texture (Ulaby, Moore and Fung, 1986; Ulaby and Dobson, 1989).

3.2.1 Backscattering Model

Two basic approaches are available when we study the scattering of electromagnetic waves from rough surfaces. In principle, the solution can be derived analytically by solving Maxwell’s equations while introducing the appropriate boundary conditions to describe the form of the surface (Beckmann and Spizzichino, 1963; Tsang,

Kong and Shin, 1985). However, this approach suffers from the difficulty of selecting and applying the correct boundary conditions that represent typical realistic surfaces (Oliver, 1984). Another method is modeling the scattering surface by an array of elemental scatterers and introducing the surface properties via the fluctuation in the cross-section or density of scatterers within this array (Jakeman, 1974; Pusey, 1977; Oliver, 1988a).

Regarding the intensity distribution of the clutter, it is most often assumed to be a Rayleigh distribution whose usual interpretation is that the clutter arises from the superposition of returns from a large number of equivalent elementary scatterers. These scatterers are independent of one another and form what is called a fully developed Gaussian speckle (or a circularly symmetric Gaussian scattering) according to the Goodman condition of this model (Goodman, 1975. Frost, 1982. Conte, Longo and Lops, 1991). When electromagnetic waves are scattered from a large array of scatterers which are randomly distributed through the resolution cell with dimensions that are large compared with the radiation wavelength, the mutual interference between independent scatterers gives rise to a total field which has a Gaussian probability distribution. Envelope detection of the field leads to a Rayleigh distributed intensity.

However, experimental data indicate that large deviations from Rayleigh statistics exist in situations such as high-resolution radar. In the high-resolution image, the number of scatterers can no longer be assumed "large" as it is assumed to be in the Goodman condition (Oliver, 1984). In a variety of high resolution coherent imaging applications, in particular radar, it has been demonstrated that many natural clutter textures can be

described by a K-distributed probability density function (PDF) (Oliver, 1986; Oliver, 1988b; Blacknell, 1994a; Conte, Bisceglie, Lops and Ricci, 1991.) given by:

$$p(I) = \frac{2}{\langle I \rangle} \left(\frac{I}{\langle I \rangle} \right)^{\gamma-1/2} \frac{1}{\Gamma(\gamma)} K_{\gamma-1} \left[2 \left(\frac{I}{\langle I \rangle} \right)^{1/2} \right] \quad (3.1)$$

where I is the detected intensity by the radar system, $\langle \rangle$ represent the ensemble average over all possible realizations of the scatterer positions within the resolution cell, $\Gamma(\gamma)$ is the gamma function of order γ , $K_{\gamma-1}$ is the modified Bessel function of order $\gamma-1$ which is called a K distribution of order $\gamma-1$ and γ represents the number of scatterers per resolution length (Oliver, 1982). Table 3.1 shows the conditions for the K-distribution target.

This K-distributed image intensity can be shown to arise from a surface having a gamma-distributed cross section, σ :

$$p(\sigma) = \frac{1}{\langle I \rangle} \left(\frac{\sigma}{\langle \sigma \rangle} \right)^{\gamma-1} \frac{1}{\Gamma(\gamma)} \exp\left(-\frac{\sigma}{\langle \sigma \rangle}\right) \quad (3.2)$$

when coherent radiation is scattered from this surface (Oliver, 1984; Medez and Escamilla, 1988; Blacknell, 1994b). When γ approaches infinity, for a wheat field, for example, the surface will be a Gaussian target (Conte, Longo and Lops, 1991).

Condition	Physical Meaning
The phases are uniformly distributed between 0 and 2π	Surface roughness is large compared to the incident wavelength
The amplitude and phase of individual scatterers are statistically independent	There is no deterministic relationship between position and strength of the scatterers relative to a wavelength
The amplitude of all scatterers in the resolution cell are approximately the same	No single or small groups of scatterers predominate
The number of scatterers in the resolution is not large	A limited complex scatterers in one resolution for high-resolution radar

Table 3.1 A summary of conditions for K-distributed target and their physical meaning.

3.2.2 Spatial ACF of the SAR Image

It is not an adequate description to merely consider the PDF of the detected intensity or the surface cross section. At least the two-point correlation properties of the clutter texture should be considered. The two-point correlation properties may be expressed by the autocorrelation function (ACF). The two-point image statistics have been proven useful in SAR image studies. Oliver (1982, 1984) used the ACF extensively in his studies of non-Gaussian scattering, and much of the current published work is based on his work.

When only the azimuth dimension of the radar image is considered, the total received field at a position x can be calculated by integrating over the scattered contributions from elements dx_1 at position x_1 relative to the receiver. Thus,

$$\varepsilon(x) = B \int_{-\infty}^{+\infty} dx_1 a(x_1) \exp[i\varphi(x_1)] h(x_1) \quad (3.3)$$

where the function $h(x_1)$ is the spatial impulse response of the imaging system, $a(x_1)$ is a complex scattering amplitude, $\varphi(x_1)$ is an additional, position-dependent, phase factor of the scatterer and B is a constant describing the energy collection of the receiver (Oliver, 1986). The received intensity is then defined as the square law detection of this field so that:

$$I(x) \equiv |\varepsilon(x)|^2 = |B|^2 \int_{-\infty}^{+\infty} dx_1 dx_2 a(x_1) a^*(x_2) \times \exp[i(\varphi(x_1) - \varphi(x_2))] h(x_1) h^*(x_2) \quad (3.4)$$

This phase decorrelation arises from the Goodman assumption in Section 3.1 that scatterers are randomly positioned within the resolution cell and the phases of the individual scatterers are statistically independent of each other. The properties of the received field and intensity for such a noise process are usually conveyed through the ensemble averages of the single-point moments or autocorrelation functions. Only the

non-zero resultant is obtained when pairs of positions are identical because of the decorrelation of the phase term. Hence the mean intensity is given by:

$$\langle I \rangle = |B|^2 \langle \sigma \rangle \int_{-\infty}^{+\infty} dx_1 |h(x_1)|^2 \quad (3.5)$$

The mean intensity depends on the imaging function and the average surface cross section defined by:

$$\langle \sigma \rangle \equiv \langle a(x) a^*(x) \rangle \quad (3.6)$$

The second-order two-point correlation property that is defined is the normalized intensity ACF given by

$$g^{(2)}(x) \equiv \langle I(x_1) I(x_1 + x) \rangle \langle I \rangle^{-2} \quad (3.7)$$

Assuming the phase decorrelation, and considering only the dominant contributions when pairs of positions are identical, one-dimensional ACF model is obtained:

$$g^{(2)}(x) = \int_{-\infty}^{+\infty} dx_1 dx_2 \{ (\langle \sigma(x_1) \sigma(x_2) \rangle \times [|h(x_1)|^2 |h(x_2 + x)|^2 + h(x_1) h^*(x_1 + x) h(x_2) h^*(x_2 + x)] \times (\langle \sigma \rangle \int_{-\infty}^{+\infty} dx_1 |h(x_1)|^2)^{-2}) \} \quad (3.8)$$

If it is assumed that the cross section of the surface is gamma-distributed, then the cross section ACF for the individual contributions may be written as (Oliver, 1985):

$$\frac{\langle \sigma(x_1) \sigma(x_2) \rangle}{\langle \sigma \rangle^2} = 1 + \frac{1}{\gamma} g_{12} \quad (3.9)$$

From Equation 3.6, the gamma-distributed cross section arises from the Gaussian-distributed scattering amplitude (Papoulis, 1965). Therefore, we may assume that the surface has a Gaussian spectrum:

$$g_{12} = \exp\left(-\frac{(x_1 - x_2)^2}{x_0^2}\right) \quad (3.10)$$

where x_0 is the backscatter correlation length.

From Chapter 2, it is known that the instrument function may be represented by a Gaussian model for simplicity. Thus, from Equation 2.18 the power response of the imaging system is:

$$h(x) = \exp\left(-\frac{x^2}{\rho^2}\right) \quad (3.11)$$

where ρ is the nominal resolution of the corresponding centred look.

From Equations 3.8, 3.9, 3.10 and 3.11, we can obtain the second-order ACF model

$$g^{(2)}(x) = 1 + \exp\left(-\frac{x^2}{\rho^2}\right) + \frac{1}{\gamma \sqrt{\frac{\rho^2}{x_0^2} + 1}} \exp\left(-\frac{x^2}{\rho^2}\right) + \frac{1}{\gamma \sqrt{\frac{\rho^2}{x_0^2} + 1}} \exp\left(-\frac{x^2}{\rho^2 + x_0^2}\right) \quad (3.12)$$

The first two terms in Equation 3.12 are the uncorrelated background component which describe the Gaussian component of the process resulting from the interference between large numbers of random scatterers filling the illumination beam. The uncorrelated background component corresponds to the speckle behavior. A similar Gaussian behavior can be derived for two point receivers viewing radiation scattered from a continuous rough surface undergoing transverse motion. The third term decays rapidly outside the instrumental width and has a similar form to the second term. The fourth term represents the effect of fluctuations in the number of scatterers within the beam. The present analysis demonstrates that it is the only non-Gaussian contribution to the process that is affected by the properties of the surface itself (Oliver, 1991).

From Equations 2.17 and 2.19, the system resolution is:

$$\rho = \frac{1}{2\pi} \left[\frac{1}{B^2} + \frac{1+n^2}{B^2(1+\eta)^2} + \frac{X^2\eta^2}{1+n^2+(1+\eta)^2} \right] \quad (3.13)$$

The previous work on the ACF model of the SAR image assumes that the image is perfectly focused. That is, the system resolution ρ is fixed in the ACF model. However, focus errors always exist in the image reconstruction process. Therefore, the texture parameters estimated from this model contain system errors resulting from the inaccurate model. In this research, an ACF model which contains a small focus error term has been constructed and it is expected that this model fits better than the old one.

3.2.3 Second-order Single Moment Model

As mentioned in Chapter 1, the single moment statistics are also a means to describe the image texture. Thus, it is another useful tool in SAR image studies. In this research, only the second order single moment statistics were studied. Oliver (1986) gave the following equation for the single moment of the image intensity:

$$I^{(2)} = \frac{\langle I^2 \rangle}{\langle I \rangle^2} = 2S_v^{(2)} \quad (3.14)$$

where $S_v^{(2)}$ is the normalized second moment for the total cross section.

Like the assumption made when the ACF model was constructed, it can be assumed that the surface has a Gaussian spectrum and instrument function. Thus,

$$\begin{aligned}
I^{(2)} &= 2 \times \int_{-\infty}^{+\infty} \int_{-\infty}^{+\infty} dx_1 dx_2 \frac{\langle \sigma(x_1) \sigma(x_2) \rangle}{\langle \sigma \rangle^2} |h(x_1)|^2 |h(x_2)|^2 \times \left(\int_{-\infty}^{+\infty} dx_1 |h(x_1)|^2 \right)^{-2} \\
&= 2 \left[1 + \frac{1}{\gamma} \sqrt{\frac{1}{\left(\frac{\rho^2}{x_0^2} + 1\right)}} \right]
\end{aligned} \tag{3.15}$$

The second order single moment has the same factor as the fourth term in the ACF model that was derived, thus, it also represents the effect of fluctuations in the number of scatterers within the beam.

3.3 Texture Classification

One important component of SAR studies is the extraction of information from the image. There are two main restrictions to this process. First, the image suffers from speckle which introduces noise that is comparable to the ideal signal. Second, the resolution of the SAR system is usually comparable with many of the objects that are to be studied. This means that, unlike many optical images, the redundancy in the SAR image is small and any image interpretation must retain all of the information in the original data. The processing of radar images always involves some prior knowledge of the scene. This prior knowledge expressed as a set of models for the scene helps to extract information from the image.

3.3.1 Texture Classification Based on the ACF Model

There are many methods to model the image texture. However, the ACF model has been demonstrated to fit a wide variety of natural clutter texture in coherent imagery (Oliver, 1989a). From Section 3.2.2, it is known that the gamma-distributed cross section of the scene is the result of a complex Gaussian random walk with order parameter γ . As a consequence of this Gaussian property, all the higher-order correlation properties of the texture can be expressed in terms of the autocorrelation function (ACF). The ACF therefore contains all the information about the surface texture. In other words, the ACF encapsulates the properties of the texture (Oliver, 1990; Ward, 1981). This suggests that texture segmentation based on ACF parameter determination may be feasible. The texture classification based on the ACF parameters has been applied to simulated SAR image data and shows good classification results (Oliver, 1990). In this research, this classification method was applied to real sea ice images. Based on the assumption that the SAR image of sea ice can be described by a K-distributed PDF, this classification algorithm is feasible.

Estimating the parameters of a statistical distribution from measured sample values forms an essential part of many signal- and image-processing tasks. In the analysis of high-resolution SAR imagery, parameter estimation is required for such tasks as segmentation and target detection (Blacknell, 1994). In Section 3.2.2, the high resolution ACF model was developed. In that model, certain assumptions were made about the functional forms of the imaging system's impulse response function and the spatial autocorrelation function of the backscatter cross section fluctuations. In the SAR image intensity ACF model, the radar parameter is the SAR resolution ρ and the texture

parameters are the backscatter correlation length x_0 and order parameter γ . Oliver and White (1990) simulated several SAR image texture based on the ACF model. Figure 3.1 shows the simulation images (512 x 512 pixels) with different values of the parameters γ and x_0 . Table 3.2 lists the values corresponding to each class.

3.3.2 Parameter Estimation Accuracy

Since the texture classification can be made based on intensity ACF parameter estimation, an estimation of the accuracy of the parameters in the ACF is essential to demonstrate the classification reliability. The estimated parameters are biased due to the finite size of the sample and due to the calculation method (Oliver, 1990). The discrimination power of the ACF based on the parameter estimation is also significantly weakened by a large ACF variance. Since we wish to perform texture classification with as small a region as possible, knowing the reliability of the estimated parameter is essential.

When the instrument function width is much less than any correlation length within the surface, the intensity ACF is approximately equal to the surface cross-section ACF except at the zero lag value (Oliver, 1989b). The subimage size must be sufficiently large for the parameters to be independent, corresponding to negligible edge effects. This situation corresponds to where the region size is large compared with any correlation lengths within the texture (Oliver, 1990). The fractional error is defined as the error in the parameter over the estimated value and this error is a measure of estimation accuracy.

Based on Oliver's work on two-dimensional estimation error, the theoretical form of the one-dimensional fractional error for x_0 and γ can be derived:

$$\langle \delta x_0 \rangle / x_0 = \sqrt{4\pi x_0 \left(1 + \frac{2}{3\gamma} + \frac{3}{16\gamma^2} \right)} / N \quad (3.16)$$

$$\langle \delta \gamma \rangle / \gamma = \sqrt{4\pi x_0 \left(1 + \frac{40}{27\gamma} + \frac{5}{8\gamma^2} \right)} / N \quad (3.17)$$

where N is the number of pixels in the azimuth direction in the image from which the parameters are estimated. These two equations imply that the fractional error in the order parameter is larger than that in the correlation length.

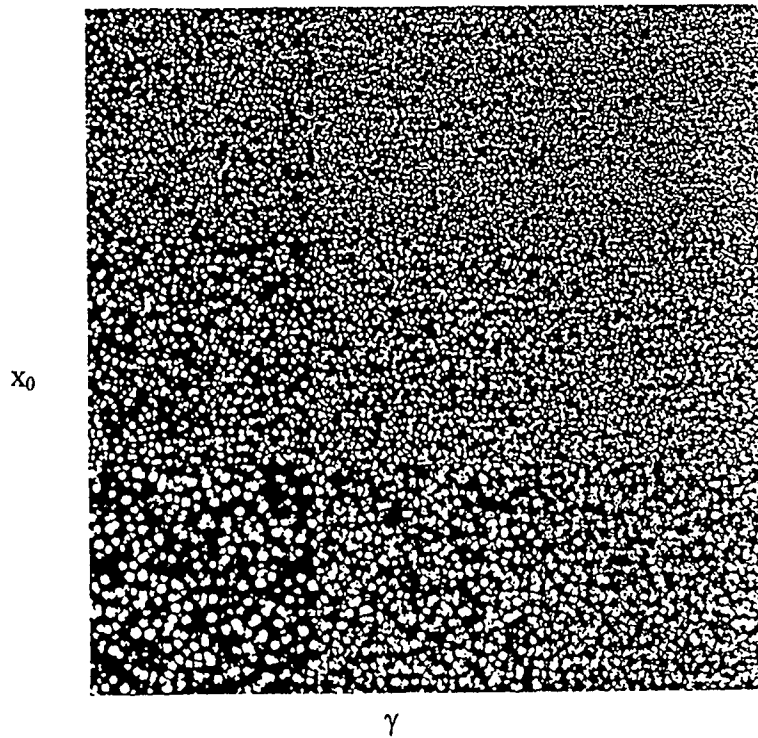


Fig 3.1 Large regions of textures with varying correlation lengths (rows) and order

parameters (columns) with classes placed as follow: $\begin{bmatrix} 1 & 4 & 7 \\ 2 & 5 & 8 \\ 3 & 6 & 9 \end{bmatrix}$. The

corresponding texture parameters for each class are listed in Table 3.2 (From Oliver and White, 1990).

	1	2	3	4	5	6	7	8	9
γ	0.09	0.09	0.09	0.50	0.50	0.50	0.72	0.72	0.72
x_0	2.52	4.00	6.55	2.52	4.00	6.55	2.52	4.00	6.55

Table 3.2 The simulation values of the texture parameters corresponding to the classes.

CHAPTER 4

EXPERIMENTAL PROCEDURE AND DATA

This chapter includes two parts. The first part describes the experiments designed in this research to test the hypotheses. The second part then reviews information about the data source used in this research. The data used is from the Labrador Ice Margin Experiment (LIMEX) which was conducted in the southern Labrador Sea. Three ice types were studied in this experiment: undeformed new ice, deformed new ice and large first year/brash ice matrix.

4.1 Experiment Design

To test the ACF model and the classification ability of the parameters in the model, three main experiments were designed using actual SAR data.

- Hypothesis 1: The ACF model which includes a focus error fits the measured image ACF better than the ACF model without a focus error. The processed band width n affects the system resolution. Large n reduces the effect of focus error but worsens the parameter estimation accuracy.

Experiment 1: The ACF parameters are estimated and the modeled ACF is compared with the measured ACF of the sea ice images in two conditions: with focus error and without focus error in the ACF model. In this experiment, n increases from 1 to 5 with increments of 1; the trial focus error η' increase from -5% to 5% with increments of 1%.

- Hypothesis 2: The fractional error, which is defined as the error in the parameter over the estimated value, can be used as a measure of accuracy for the parameter estimation. The theoretical and experimental fractional errors of the texture parameters are close. The fractional errors in the parameters are small so that the estimated parameters are reliable.

Experiment 2: The theoretical and experimental fractional error of the selected targets in six channels are compared. In this experiment n equals 1 and the matched filter is not adjusted to perfect focus when the image is reconstructed (the trial focus error $\eta'=0.00$).

- Hypothesis 3: The texture parameters of the SAR image of sea ice can be used to perform sea ice classification.

Experiment 3: The two estimated parameters (γ and x_0) for different scenes are compared. Each target is then divided into subareas using a rectangular window where γ and x_0 are estimated for each subarea. The purpose of this experiment is to find out whether texture classification based on ACF parameter fitting is feasible.

4.2 Experimental Data Acquisition

The Labrador Ice Margin Experiment (LIMEX) is an international, multidisciplinary, field program conducted in the southern Labrador Sea between March 4 and April 4 of 1989. LIMEX was divided into two phases whose locations are shown in

Figure 3.2. More detailed information about this experiment can be found in the science plan (Raney and Argus, 1988), the operations plan (Argus, 1989) and the data report (Raney et al., 1989).

Phase I of LIMEX focused on the microwave signatures and physical properties of the sea ice and snow. Phase II focused on the microwave signatures of ocean gravity waves, and the physical and mechanical properties of the ice being forced by these waves. The data used in the research were collected in phase I.

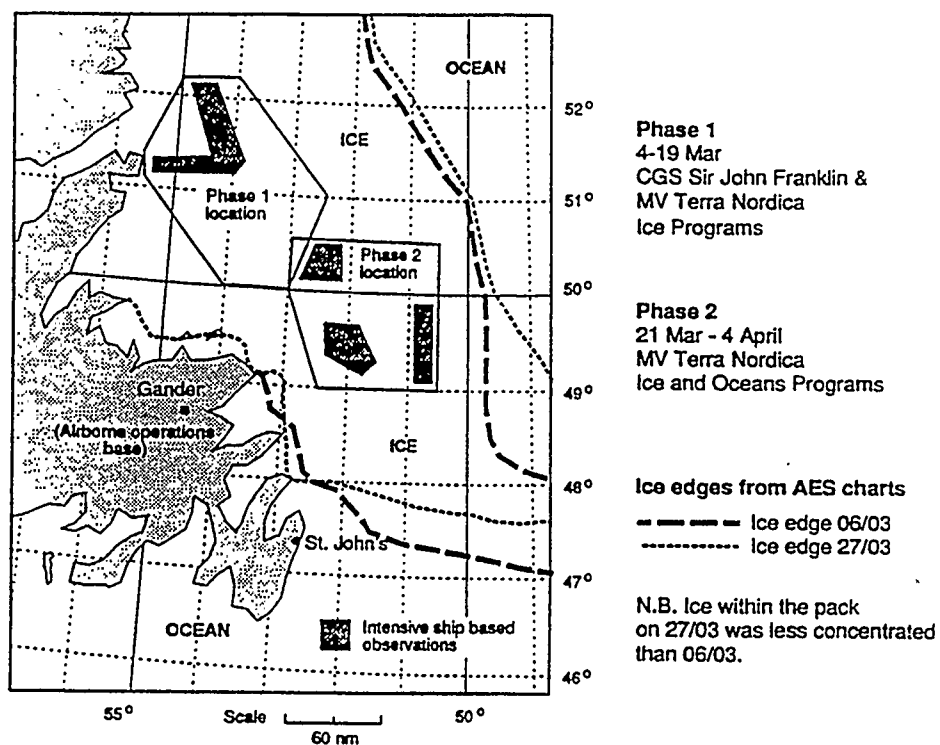


Figure 4.1 Location of LIMEX experimental sites, from Raney et al., 1989.

The main remote sensing instrument in LIMEX was the synthetic aperture radar system operated by the Canada Centre for Remote Sensing (CCRS). This SAR system included two subsystems, one operating at C-band (5.3 GHz), the other at X-band (9.25 GHz). Both subsystems were capable of transmitting and receiving H or V polarized microwaves. Therefore, each has three channels: HH, HV, VV. Thus six channels of image data were obtained for each target. In the meantime, a mapping camera was used to acquire the optical image data of the same scene.

4.2.1 SAR System

The SAR imaging system operated in LIMEX is the Integrated Radar Imaging System (IRIS) developed by MacDonald Dettwiler and Associates. This SAR system was carried on the CCRS Convair-580 aircraft. The main technical specifications for the CCRS IRIS in high resolution mode are listed in Table 4.1.

4.2.2 Aerial Photography

The Convair-580 also carried a Wilde RC-10 mapping camera with black and white film. The image centre of the camera are fixed to the nadir point and the scale of the photographs was 1:2000. The aerial photographs were used to estimate the ice types presented in the SAR imagery by human visualization. The thinner ice is more transparent to the optical frequencies, thus it appears darker in the black and white film. The aerial photography also showed the size and shape of the floes and ice pancakes.

4.3 Studied Scene

In this research three typical types of ice are studied. The location of these sea ice targets are labeled A, B and C in Figure 4.2. These targets' surface statistics vary from Gaussian to non-Gaussian.

4.3.1 Target A: Undeformed New Ice

Figure 4.3 is the aerial photograph of the undeformed new ice. New ice is made up of frazil crystals. In calm conditions, the frazil crystals quickly freeze together to form a solid, continuous ice cover. This ice sheet is quite thin and fragile. Since the penetration depth, which is defined as the depth at which the power of the electromagnetic field falls by $1/e$, is less than a centimetre (Ulaby, Moore and Fung, 1986), the scattering from the new ice is from the surface. Therefore, the surface geometry determines the spatial variations of the SAR return. The undeformed floes are rafted onto each other which causes bright image features in the aerial photography. This type of ice should yield non-Gaussian statistics (Collins, 1993).

4.3.2 Target B: Deformed New Ice

The new ice is so fragile that it easily deforms as the result of wind and wave action. When the large new ice floes break, they break into small angular ice floes with dimensions of 1-2 metres. The edge rafting of the small floes show up as many bright lines in the aerial photographs with sharp intersections. This can be seen in Figure 4.4 which is the aerial photography of deformed new ice. This target is still new ice, therefore

the surface geometry determines the spatial variations of the SAR return. The relative uniformity of the ice pancakes suggests that it is a Gaussian target.

4.3.3 Target C: Large First Year/Brash Ice Matrix

The thickness of the first year ice is more than 30 cm. The bumping of the ice floes causes the breaking off of small ice pieces which further break into smaller fragments (on the order of a centimeter). The mixture of the small fragments and sea water is called brash ice.

The dimension of the floes for target C is about 10-50 m. Figure 4.5 is the aerial photography for this target. A previous study shows that the statistical behavior of this target is strongly non-Gaussian.

Transmitter	C		X	
frequency	5.30 GHz		9.25 GHz	
radiated peak power	34.3 KW		3.8 KW	
average power coupling	-51.8dB		-53.1 dB	
polarization	H or V		H or V	
chirp length	7 μ s		15 μ s	
chirp coding	non-linear FM		linear FM	
Receiver				
noise figure	5.2 dB		5.3 dB	
compressed pulse width	38 ns		32 ns	
3 dB range resolution	5.7 m		4.8 m	
Antennae				
polarization	H	V	H	V
azimuth beam width (one way)	3.0°	3.3°	1.4°	1.4°
elevation beam width (one way)	28.0°	25.0°	26.0°	26.0°
gain	26.4 dB	24.8 dB	28.0 dB	28.5 dB
System				
noise equivalent	-40 dB		-30 dB	
A/D converter dynamic range	30 dB / 6 bit			
range sample spacing	4 m			
recorded samples	Full Swath: 4096		Half Swath: 2048	

Table 4.1 The main technical specifications for the CCRS IRIS in high resolution mode.

(Collins, 1993).

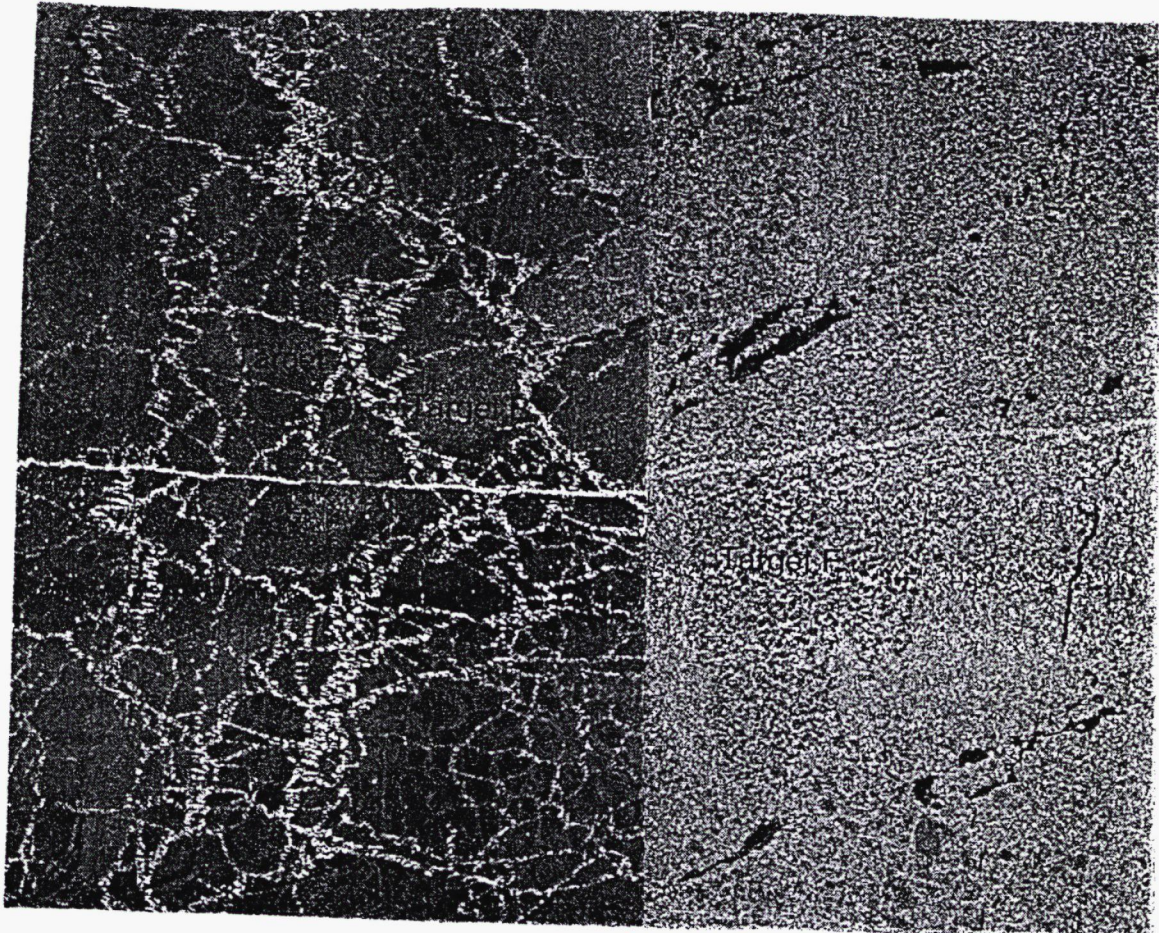


Figure 4.2 The overview of the location of the studied area. This is CCRS CHH SAR image data. The Target F in the image is named Target C in this thesis.

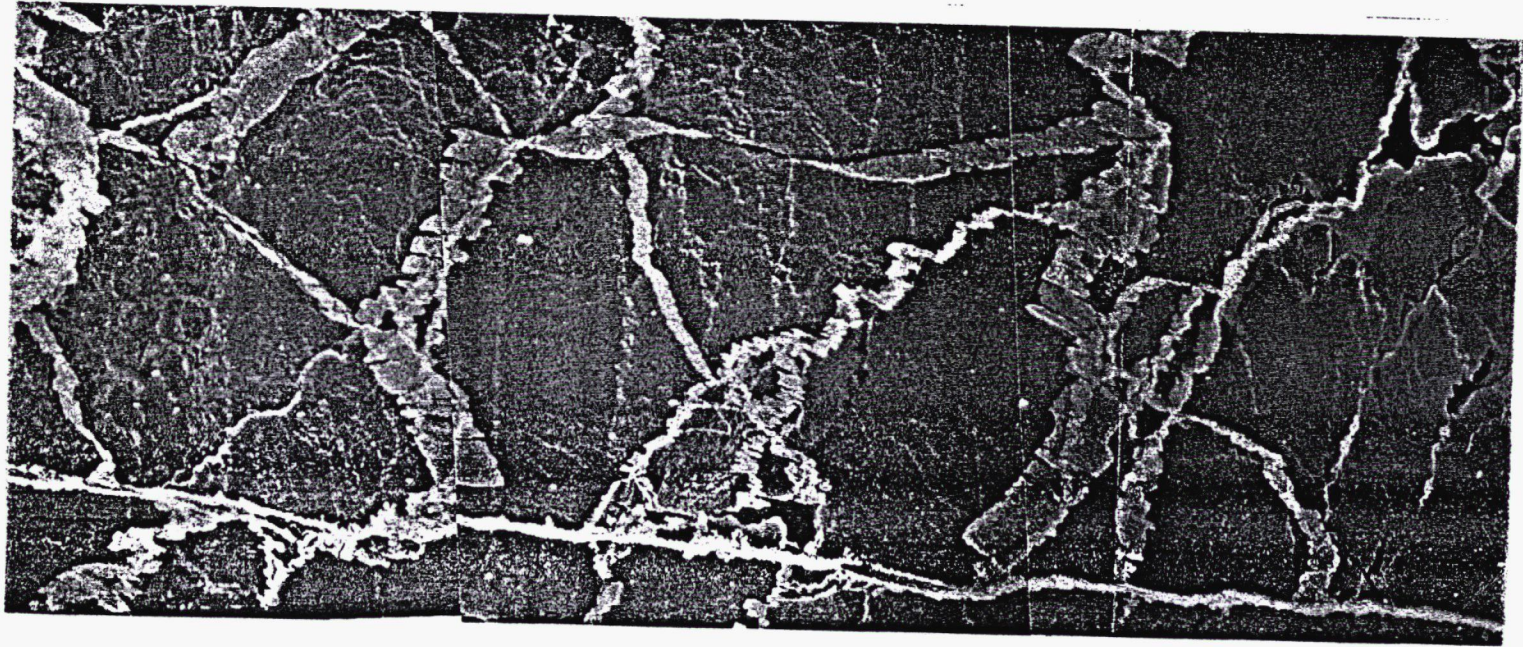


Figure 4.3 Target A: Undeformed new ice.

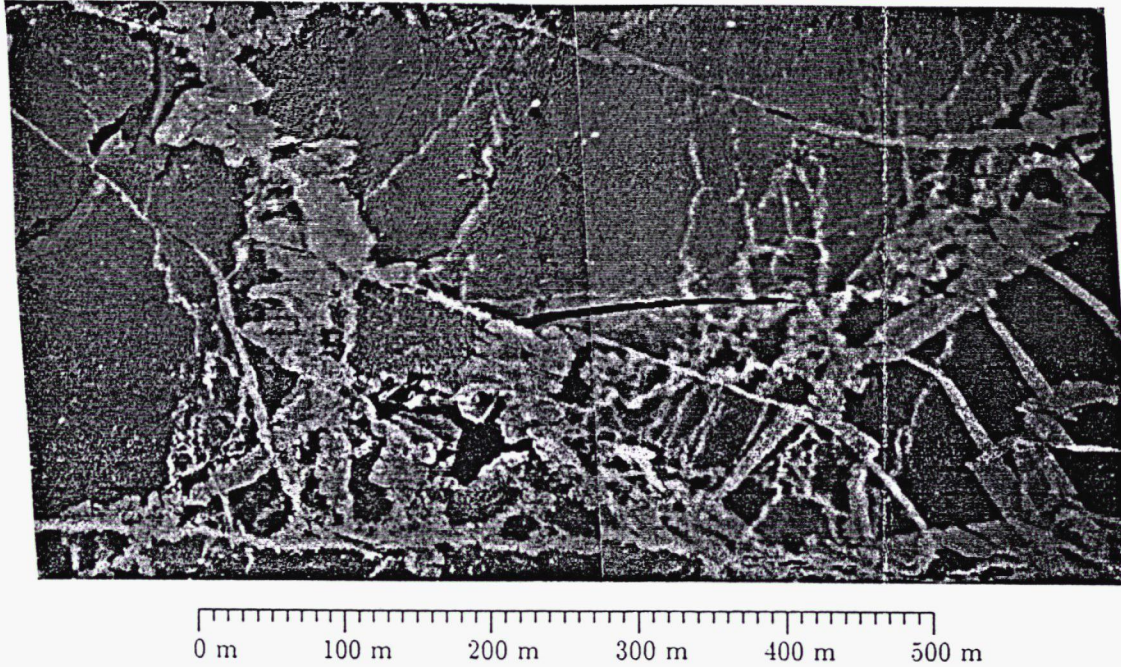


Figure 4.4 Target B: Deformed new ice.

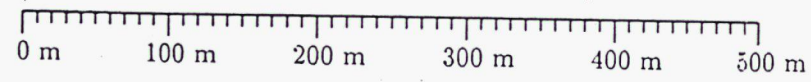
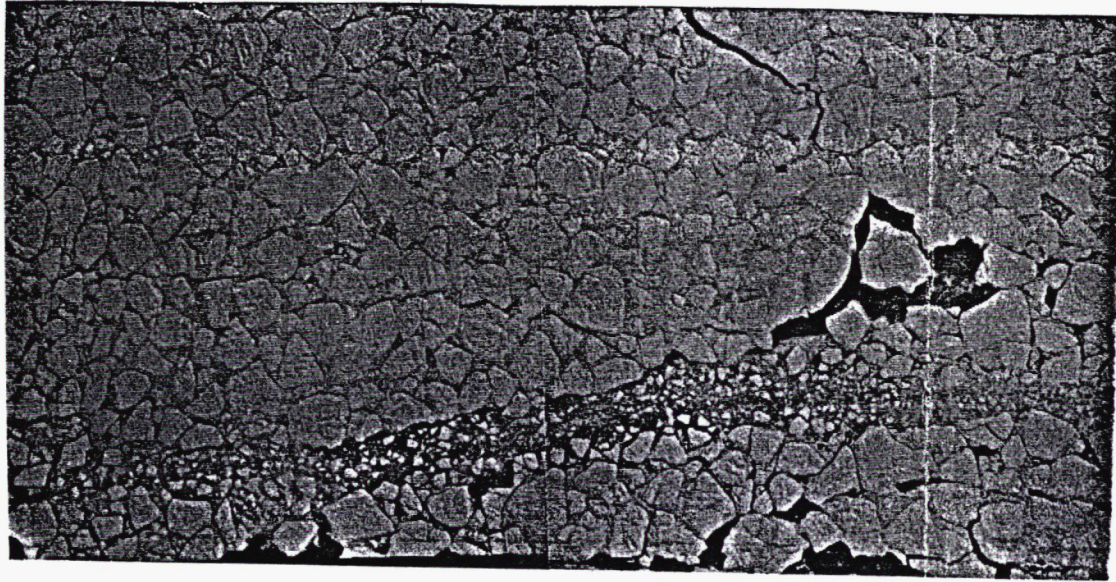


Figure 4.5 Target C: Large first year/brash ice matrix.

CHAPTER 5

RESULTS AND DISCUSSION

This chapter presents all the experimental results and discussion. The results show that the ACF model including the focus error fits better than the ACF model not including the focus error to the measured ACF of the SAR image of the sea ice. The processed bandwidth affects the performance of the ACF model through the system resolution. The estimation error in the ACF parameters is small and the sea ice classification based on the ACF parameter estimation is feasible.

5.1 Nonlinear Model Fitting Method

In the ACF model we developed in the last chapter (Equation 3.12) there are three parameters: system resolution ρ , order parameter γ and correlation length x_0 . The model depends nonlinearly on these three parameters. In the fitting procedure, a least squares solution is adopted. That is, the merit function χ^2 is defined and the best-fit parameters are determined by its minimization. Providing a set of trial values, a procedure was developed to improve this trial solution and output a new set of values. The procedure is then repeated until χ^2 stops decreasing or effectively stops. The output of the loop is the fitting result -- a new set of values.

Let a be the set of parameters: ρ , γ and x_0 . The model to be fitted is

$$y = y(x; \mathbf{a}) \quad (5.1)$$

where x is the set of lag distances. The χ^2 merit function is (Press et al., 1992)

$$\chi^2(\mathbf{a}) = \sum_{i=1}^N \left[\frac{y_i - y(x_i; \mathbf{a})}{\sigma_i} \right]^2 \quad (5.2)$$

where y_i is the estimated ACF at the i th lag; σ_i is the standard deviation of the estimated ACF at the i th lag.

The Levenberg-Marquardt method was used in this research to perform the nonlinear fitting. If \mathbf{a}_{next} is the new set of parameters and \mathbf{a}_{cur} is the current trial values for the parameters, then

$$\mathbf{a}_{\text{next}} = \mathbf{a}_{\text{cur}} - \mathbf{K} \times \nabla \chi^2(\mathbf{a}_{\text{cur}}) \quad (5.3)$$

Where \mathbf{K} is a constant that is small enough to keep the downhill direction.

The Levenberg-Marquardt method is developed based on the above idea. The routine outputs the fitted parameters and the covariance matrix of the parameters. The Levenberg-Marquardt method works very well in practice and has become the standard of nonlinear least-squares routines (Press et al., 1992).

5.2 Comparison of the Two ACF Models

The measured ACF in the image was calculated in two steps. First the normalized intensity ACF was calculated in the azimuth direction at a certain range position. This procedure was repeated until all range positions in the image were completed. Then these autocorrelation vectors were averaged.

Equation 3.12 was fitted to ACF measurement. Two cases were considered: ACF model without a focus error and ACF model with a focus error. In the first case, the system resolution was calculated by Equation 3.13 in which $\eta=0.00$ and only the order parameter and correlation length were estimated. In the second case, all three parameters were estimated. Figure 5.1-5.4 show the measured ACF and modeled ACF.

The merit function χ^2 reflects how well the model fits the measured ACF. Table 5.1 lists χ^2 values for different n using the Levenberg-Marquardt fitting methods.

From Figures 5.1-5.4 and Table 5.1, we can see that the ACF model fits the measured ACF model quite well at different values of processed bandwidth n and trial focus error η' . The modeled ACF including the focus error provides a better fit to the estimated ACF than that not including the focus error. In Figure 5.1 the fitted results of the two models are very similar at $\eta'=0.00$. However, there is more difference between the two sets of ACF at $\eta'=0.00$ in Figure 5.2. This is because the perfect focus of target A, channel C_{HH} when $n=1$ occurs at $\eta=0.00$, while the perfect focus of Target A, channel X_{HV} occurs at $\eta=0.025$.

Near the zero lag the modeled ACF is quite small compared with the measured ACF. At the zero azimuth lag distance, the intensity ACF $g(0)$ equals the mean of the square of the intensity. When we construct the SAR imaging system model, we neglected the side lobe effect. Some energy is lost with this energy envelope, therefore the modeled $y(0)$ is smaller than the measured $y(0)$.

5.3 The Effect of Processed Bandwidth on the ACF Model

From Table 5.1, we can see that as the processed bandwidth n increases, χ^2 becomes smaller. However the χ^2 of some channels increases dramatically at $n=5$ because the subaperture is too small to get enough information to represent the characteristics of the scene. Thus, the model fails to represent the image ACF at large n .

Figure 5.5 shows the modeled ACF including focus error and not including focus error at different n . Figure 5.5 indicates that as n increases, the curve of the fitted ACF including focus error and the curve of fitted ACF not including focus error become closer. This effect is more distinctive at the X band with n as large as 5 than at C band. From Equation 3.13, we can see the system resolution with a focus error and the system resolution without a focus error of the X band are closer than those of the C band with n as large as 5. Overall large n can reduce the effect of the focus error. This result can also be seen in Table 5.1 which is consistent with our model.

In the later study, the ACF model with focus error was used because of the better fit. That is, the Equation 3.12 was fitted to ACF measurements and the three parameters were estimated.

5.4 The Effect of Processed Bandwidth on the Parameters of the ACF Model

5.4.1 The Effect of Processed Bandwidth on the System Resolution

Table 5.2 lists the system resolution at different n for each channel of Target A and C. The system resolution was estimated by fitting the ACF model to the measured ACF. The matched filter of the imaging system (Equation 2.9) indicates that the fractional look of the image is a low pass filter. That is, the larger the n , the greater the loss of the high frequency information. The experimental results indicate that the low pass filter changes the system resolution. The smaller the bandwidth of the filter, the larger the system resolution. The change of the system resolution with n is consistent with the theory.

The system resolution computed from Equation 3.13 is the same for all targets in a certain channel (Collins, 1993). However the values in Table 5.2 indicate that the system resolution depends not only on the system parameters but also on the target. As mentioned in Chapter 3, the more Gaussian the scene, the narrower the correlation function. Thus the system resolution of Target A is smaller than that of Target C as Target A is more Gaussian than Target C.

5.4.2 The Effect of Processed Bandwidth on the Order Parameter

Table 5.3 lists the order parameters at different n for each channel of Target A and C with the trial focus error $\eta' = 0.00$. As seen from this table, the order parameter of Target A for the three X band channels increases as n increases. The C_{VV} also has the same change. This means that the number of scatterers per resolution cell increases and

the image texture becomes more Gaussian as n increases. It is seen that the texture of the moderate Gaussian target A at $n=5$ has too much uncertainty. The image is only composed of speckles and part of the texture information is lost. At this point, the ACF model seems to fail to represent the texture properties of the image. Also seen from this table, the order parameter of channels C_{HH} and C_{HV} decreases when n increases from 1 to 5. This result implies that the added scatterers with the increase of the resolution cell are correlated to the original ones. The destructive effect results in a smaller amount of scatterers in a resolution cell.

For the non-Gaussian target C, the order parameters do not increase as fast as those of the moderately non-Gaussian target A when n increases from 1 to 5. Thus for the non-Gaussian target, a larger n can be applied to save the computation load while most of the texture information of the image is kept.

Comparing all the six channels of the two targets, it is found that the channels C_{VV} and X_{VV} are more speckled.

5.4.3 The Effect of Processed Bandwidth on the Correlation Length

Table 5.4 lists the correlation length at different n for each channel of Target A and C with the trial focus error $\eta'=0.00$. It can be seen from this table that the correlation length increases as n increases from 1 to 5. As a low pass filter, the fractional look of the image reduces the system resolution and reduces the high frequency information in the image. From Figure 3.1 it can be seen that the loss of the fine structural information in the image increases the correlation length of the image texture. The correlation length of

target A at the X band is much larger than the image size (1024 pixels in azimuth direction) at $n=5$. For target C, the same parameter with channels X_{HV} and X_{VV} is also much larger than the image size (2048 pixels in azimuth direction) at $n=5$. When constructing the ACF model, it is assumed that the correlation length is much smaller than the image size. Thus, the large correlation length at these channels makes the ACF model no longer hold true. Therefore, the fitted result based on the ACF model is not reliable at $n=5$.

5.5 The Standard Deviation of the Estimated Parameters

When we use the Levenberg-Marquardt methods to perform the ACF model fitting to the measured ACF, the routine not only outputs the three estimated parameters but also outputs the covariance matrix. Table 5.5 and Table 5.6 list the standard deviation of the order parameters and correlation length which are from the covariance matrix. The standard deviation of the parameters is small except when $n=5$. This result implies that the estimated parameters are reliable. However, although a large n can decrease the computation load, it reduces the accuracy of the estimated parameters.

5.6 Second-order Single Moment

Table 5.7 lists the second-order single moment in azimuth direction at different n for each channel of Targets A and C with the trial focus error $\eta'=0.00$. First the single moment values at a certain range position were measured in the azimuth direction. This procedure was repeated until all range positions in the image were calculated. Then these

values were averaged to get the mean measured second-order single moment and the standard deviation. Compared with Table 5.3, the change of the second-order single moment has a certain relationship with the change of the order parameter. An increase of the order parameter is accompanied by a decrease of the second-order single moment. This is because a larger number of scatterers results in a greater destructive effect. The most specked channels C_{VV} and X_{VV} have the weakest image intensity. These results are consistent with our single moment model (Equation 3.15).

target	n	CHH	CHV	CVV	XHH	XHV	XVV
A	1	0.5554	1.0271	1.4100	1.0853	1.9154	0.4162
		1.0591	11.8032	77.8593	20.0669	35.6120	27.5020
	3	0.3255	0.5207	0.6984	0.5838	0.1267	0.1663
		2.3926	7.5997	69.4026	29.9510	32.7500	50.0668
	5	0.3218	0.4569	45.4928	41.4032	39.2411	52.1095
		7.3805	7.7910	79.8412	49.2674	44.0347	57.6210
C	1	0.5121	1.0988	1.4988	0.4313	2.1593	0.7579
		2.8152	9.7061	1.7827	6.9720	32.1740	5.8735
	3	0.3799	1.0998	0.3931	0.3975	1.5182	0.4613
		3.7329	9.7491	10.4055	12.9369	32.4258	21.3860
	5	0.5614	0.8780	0.3733	0.4092	31.9865	28.4481
		5.0184	11.3162	24.0905	17.1500	33.3549	30.5080

Table 5.1 Merit function χ^2 of Target A and Target C with trial focus error $\eta'=0.00$. The first row of each n represents the results of the ACF model including the focus error in which the system resolution is estimated by fitting the ACF model to the measured ACF. The second row of each processed bandwidth n represents the results of the ACF model not including the focus error in which the system resolution is fixed assuming the image is perfectly focused.

target	n	CHH	CHV	CVV	XHH	XHV	XVV
A	1	0.7277	0.5734	0.4374	0.6301	0.5528	0.6150
	3	1.2207	1.0855	0.8541	1.2448	1.2182	1.1837
	5	1.7914	1.7161	2.2285	3.3044	3.5656	3.3630
C	1	0.6064	0.5597	0.5688	0.7162	0.6554	0.7022
	3	1.1291	1.0570	0.9590	1.2740	1.3035	1.2926
	5	1.8152	1.6900	1.4522	1.9064	3.3925	3.3796

Table 5.2 The system resolution at different processed bandwidths n for each channel of targets A and C with the trial focus error $\eta'=0.00$. The system resolution is estimated by fitting the ACF model to the measured ACF.

target	n	CHH	CHV	CVV	XHH	XHV	XVV
A	1	9.8	8.3	23.1	12.1	11.8	23.4
	3	7.4	5.8	37.2	14.2	12.2	26.9
	5	6.2	4.8	8.0e+	1.0e+93	1.8e+	5.5e+
				158		100	156
C	1	1.71	2.12	6.9	2.17	3.19	5.37
	3	1.67	2.04	7.0	2.29	3.34	5.7
	5	1.70	2.14	6.8	2.24	6.81	28.4

Table 5.3 The order parameter at different processed bandwidths n for each channel of targets A and C with the trial focus error $\eta'=0.00$. The order parameter is estimated by fitting the ACF model to the measured ACF.

target	n	CHH	CHV	CVV	XHH	XHV	XVV
A	1	10.04	11.01	10.26	10.67	11.44	10.30
	3	11.07	14.4	15.62	15.0	17.4	10.76
	5	11.6	15.0	26	892	1.2e+3	26
C	1	14.5	13.2	10.85	15.4	11.85	12.29
	3	14.8	13.7	14.05	16.4	14.6	14.0
	5	15.3	15.0	13.7	16.3	7.1e+	1.4e+
						134	145

Table 5.4 The correlation length at different processed bandwidths n for each channel of targets A and C with the trial focus error $\eta'=0.00$. The correlation length is estimated by fitting the ACF model to the measured ACF.

target	n	CHH	CHV	CVV	XHH	XHV	XVV
A	1	4.7564	2.0885	10.5239	4.5276	3.6736	15.5963
	3	3.4331	1.6877	31.1517	8.1296	5.0364	27.6584
	5	3.2785	1.6964	Inf	Inf	Inf	Inf
C	1	0.2326	0.2302	1.6619	0.2804	0.2750	0.9071
	3	0.2850	0.2837	1.8944	0.3674	0.4312	1.3306
	5	0.3868	0.3892	2.1448	0.4491	Inf	Inf

Table 5.5 The standard deviation of the order parameter at different processed bandwidths n for each channel of targets A and C with the trial focus error $\eta'=0.00$. The standard deviation of the order parameter was the output of the Levenberg-Marquardt routine when the ACF model was fit to the measured ACF.

target	n	CHH	CHV	CVV	XHH	XHV	XVV
A	1	0.5533	0.4483	0.2674	0.4227	0.4535	0.3574
	3	0.8416	1.3341	0.8083	1.2182	1.5812	0.4955
	5	1.2143	2.0613	Inf	Inf	Inf	Inf
C	1	2.3432	1.2577	0.4323	2.1712	0.5253	0.5939
	3	2.9103	1.7243	0.9332	2.8055	1.1911	1.0397
	5	3.8272	2.4531	1.1153	3.2175	Inf	Inf

Table 5.6 The standard deviation of the correlation length at different processed bandwidths n for each channel of Target A and C with the trial focus error $\eta'=0.00$. The standard deviation of correlation length was the output of the Levenberg-Marquardt routine when the ACF model was fit to the measured ACF.

target	n	CHH	CHV	CVV	XHH	XHV	XVV
A	1	2.54	2.27	2.056	2.24	2.17	2.11
		± 0.8730	± 0.1654	± 0.0931	± 0.2027	± 0.1367	± 0.1991
	3	2.6	2.41	2.046	2.23	2.18	2.11
		± 1.0589	± 0.2643	± 0.0977	± 0.2175	± 0.2004	± 0.2029
	5	2.6	2.51	2.04	2.18	2.14	2.09
		± 1.0600	± 0.4082	± 0.1361	± 0.1975	± 0.2324	± 0.1956
C	1	3.36	3.07	2.42	3.04	2.73	2.51
		± 0.5234	± 0.2897	± 0.6184	± 0.3471	± 0.1596	± 0.4530
	3	3.46	3.17	2.42	3.02	2.73	2.51
		± 0.6501	± 0.3511	± 0.3787	± 0.3714	± 0.1952	± 0.5007
	5	3.47	3.13	2.39	3.00	2.70	2.47
		± 0.6994	± 0.2881	± 0.2945	± 0.4144	± 0.2371	± 0.3926

Table 5.7 The second-order single moment at different processed bandwidths n for each channel of targets A and C with the trial focus error $\eta'=0.00$. These results are mean values of the measured second-order single moment in the azimuth direction.

5.7 Texture Classification of the Sea Ice

5.7.1 Estimated Parameters of the Three Ice Types

Table 5.8 lists the estimated order parameters and correlation length for targets A, B and C. The azimuth length of the three images are all 1024 pixels so that the estimated values are comparable. To achieve the highest resolution, the number of looks was chosen to be 1.

The order parameters of Target A and Target C are quite different in all six channels. The order parameters of Target B and Target C are also quite different in all six channels. At channel X_{HH} and channel X_{VV} , Target B appears more Gaussian than Target A. At channel C_{VV} and channel X_{HV} , Target A appears more Gaussian than Target B.

At channel C_{HH} and channel C_{HV} , the order parameters of Target A and Target B are almost the same. However, the correlation lengths of the two targets in the two channels are quite different. The size of the ice floes for Target B is much smaller than that for Target A and Target C. The correlation length of Target B is the smallest among the three targets except at channel C_{VV} and X_{VV} . The correlation length of the three targets is quite close at C_{VV} and X_{VV} . From Section 5.3, it is known that the image appears more speckled in the two channels for which some target texture information of the target was lost. The correlation length of target A and C are very close in all six channels.

The results in Table 5.8 show that the order parameter and correlation length in the ACF model can be used to perform texture classification of the three types of sea ice.

5.7.2 Fractional Error of the Estimated Value

Table 5.9 lists the theoretical prediction and experimental result of the fractional error of targets A, B and C. The error in correlation length is much smaller than that in order parameter. This result is consistent to our fractional error models (Equations 3.16 and 3.17). Oliver (1989) found that the error in the order parameter was dominated by the variation in the zero-lag value between different ACF estimation. In this case, the error is caused by the variation in the zero-lag value between different ACF values in different range position, while the error in the correlation length depended on the fluctuations between different lag values of the same estimate. From figures 5.1-5.4 it can be seen that the fluctuations between different lag values is quite small which results in a small error in the correlation length. Therefore texture classification based on the correlation length is more reliable than that based on the order parameter.

For moderately non-Gaussian Target A, the theoretical predictions and the experimental results show some similarity except in the case of the order parameter for channels C_{HV} and X_{VV} . For Gaussian Target B, there is a greater difference between the theoretical predictions and the experimental results of the order parameters. The experimental fractional error of these six channels seems to have a random distribution. The theoretical predictions and the experimental results of the order parameters of Target C are quite close. These results demonstrate that the fractional error in the order parameter of the strongly non-Gaussian target is smaller than that for Gaussian targets which means that the variation in the zero-lag value between different ACF values is much smaller. However, the fractional error in the correlation length of this target type is

relatively large which means that the fluctuations between different lag values of the same estimate are relatively large. This phenomenon is consistent with the general properties of the autocorrelation function.

The experimental fractional errors in the correlation length show less fluctuation among the six channels than the fractional errors in the order parameters. This is because the standard deviation in the correlation length is much smaller than that in the order parameter. The experimental results are calculated using the estimated values. Thus, there is more dissimilarity in the experimental fractional error of the order parameter.

5.7.3 Texture Parameters of the Subimage

When texture classification is done, this process should be performed with as small a region as possible. However, the finite image size will bias the parameters estimated from the ACF model that is based on an assumption that the image size is infinite. Therefore, the image size chosen must be much larger than the correlation length. All the three targets were divided into subareas using a window of 128 pixels in azimuth direction. If the window size is too small, for example 32 pixels in azimuth direction, the error in the estimated parameters is large and the result is inaccurate and unreliable because of the bias introduced by the finite region size. The fractional error in the two texture parameters is of the same level as that listed in Table 5.9 which is quite small.

Figures 5.6 and 5.7 show the histograms of γ of subimages, figure 5.8 shows the histogram of x_0 of subimages where γ and x_0 of the subareas both have normal distributions. Target A is made up very large ice blocks, hence one subareas' texture may

be totally different from others. For example, the subimage may only contain the ice edge or the center of the ice block. Thus, the histogram of γ for Target A has more than one peak. However, the histogram of γ for targets B and C has only one peak (see figures 5.6 and 5.7).

Figure 5.7 illustrates that Target B and Target C can be separated by the order parameter γ of channel C_{HV} . Figure 5.8 indicates that Target A and Target B can be separated by the correlation length x_0 of channel C_{HH} and that Target B and Target C can be separated by the correlation length x_0 of channel C_{HH} . Figure 5.9 shows the histogram of γ of subimages of channel C_{HH} . From this histogram, we find that Target A and Target B or Target C can be separated by the order parameter γ of channel C_{HH} . However the probable value of the texture parameter of different sea ice types overlaps. This reduces the accuracy of classification. The error in the order parameter and correlation length makes the performance even poorer. Therefore other algorithms are necessary in addition to the ACF model when we perform classification with a small region.

	A		B		C	
	γ	x_0	γ	x_0	γ	x_0
CHH	9.8 ± 4.7561	10.04 ± 0.5533	9.0 ± 8.1783	7.23 ± 0.4973	3.12 ± 0.6047	10.88 ± 0.8530
CHV	8.3 ± 2.0885	11.01 ± 0.4483	8.5 ± 2.0796	9.07 ± 0.3137	2.99 ± 0.5141	10.81 ± 0.8219
CVV	23.1 ± 10.5288	10.26 ± 0.2674	17.1 ± 4.5852	10.48 ± 0.2493	7.9 ± 1.7422	10.40 ± 0.4263
XHH	12.1 ± 4.5276	10.67 ± 0.4227	14.5 ± 6.5308	9.04 ± 0.3110	4.4 ± 1.1125	11.3 ± 0.8027
XHV	11.8 ± 3.6736	11.44 ± 0.4535	8.1 ± 1.8908	8.57 ± 0.2818	4.40 ± 0.8971	10.63 ± 0.6337
XVV	23.4 ± 15.5963	10.30 ± 0.3574	31.7 ± 25.5724	10.58 ± 0.3882	7.2 ± 2.0735	9.99 ± 0.4916

Table 5.8 The texture parameters of γ and x_0 and their standard deviation, azimuth length:

1024, $n=1$, the trial focus error $\eta'=0.00$.

		$\delta\gamma/\gamma$		$\delta x_0/x_0$	
channel		theoretical prediction	experimental result	theoretical prediction	experimental result
A	CHH	0.4148	0.4861	0.0327	0.0551
	CHV	0.4404	0.2510	0.0344	0.0407
	CVV	0.4028	0.4554	0.0324	0.0261
	XHH	0.4225	0.3734	0.0335	0.0396
	XHV	0.4380	0.3122	0.0347	0.0397
	XVV	0.4034	0.6658	0.0324	0.0347
B	CHH	0.4322	0.9081	0.0340	0.0688
	CHV	0.4860	0.2444	0.0381	0.0346
	CVV	0.5031	0.2683	0.0402	0.0238
	XHH	0.4693	0.4515	0.0375	0.0344
	XHV	0.4742	0.2329	0.0371	0.0329
	XVV	0.4941	0.8069	0.0401	0.0367
C	CHH	0.2357	0.1937	0.0649	0.0784
	CHV	0.2371	0.1721	0.0650	0.0760
	CVV	0.2033	0.2215	0.0596	0.0410
	XHH	0.2241	0.2553	0.0635	0.0728
	XHV	0.2198	0.2036	0.0623	0.0596
	XVV	0.2011	0.2898	0.0587	0.0492

Table 5.9 The theoretical prediction and experimental results of the fractional error for targets A, B and C. The azimuth size of the target area is 1024, $n=1$, the trial focus error $\eta'=0.00$.

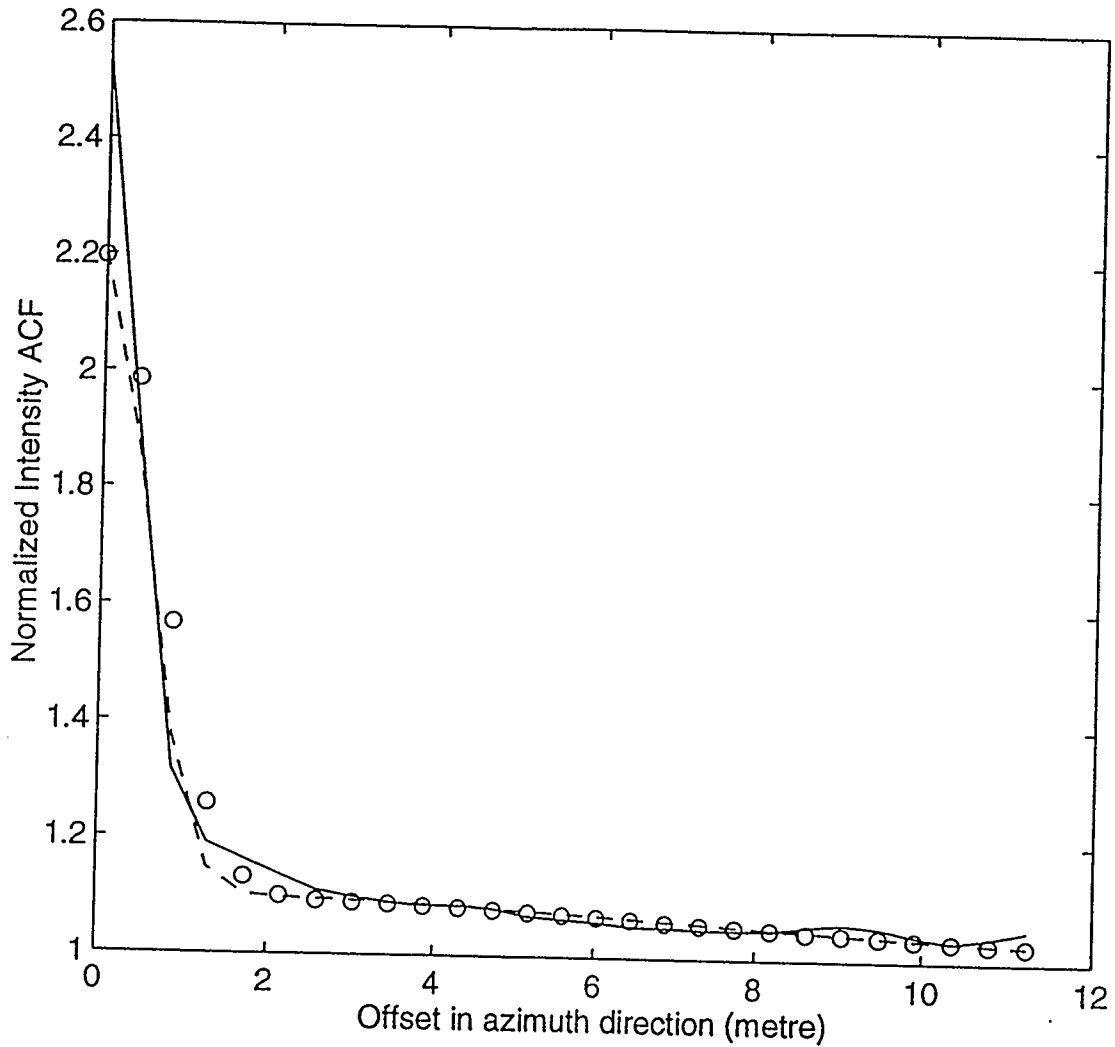


Figure 5.1 Measured and modeled ACF. Target A, Channel CHH, $n=1$, the trial focus error $\eta'=0.00$. The solid line represents the measured ACF; the dashed line represents the modeled ACF with focus error; the circles represent the ACF model not considering the focus error.

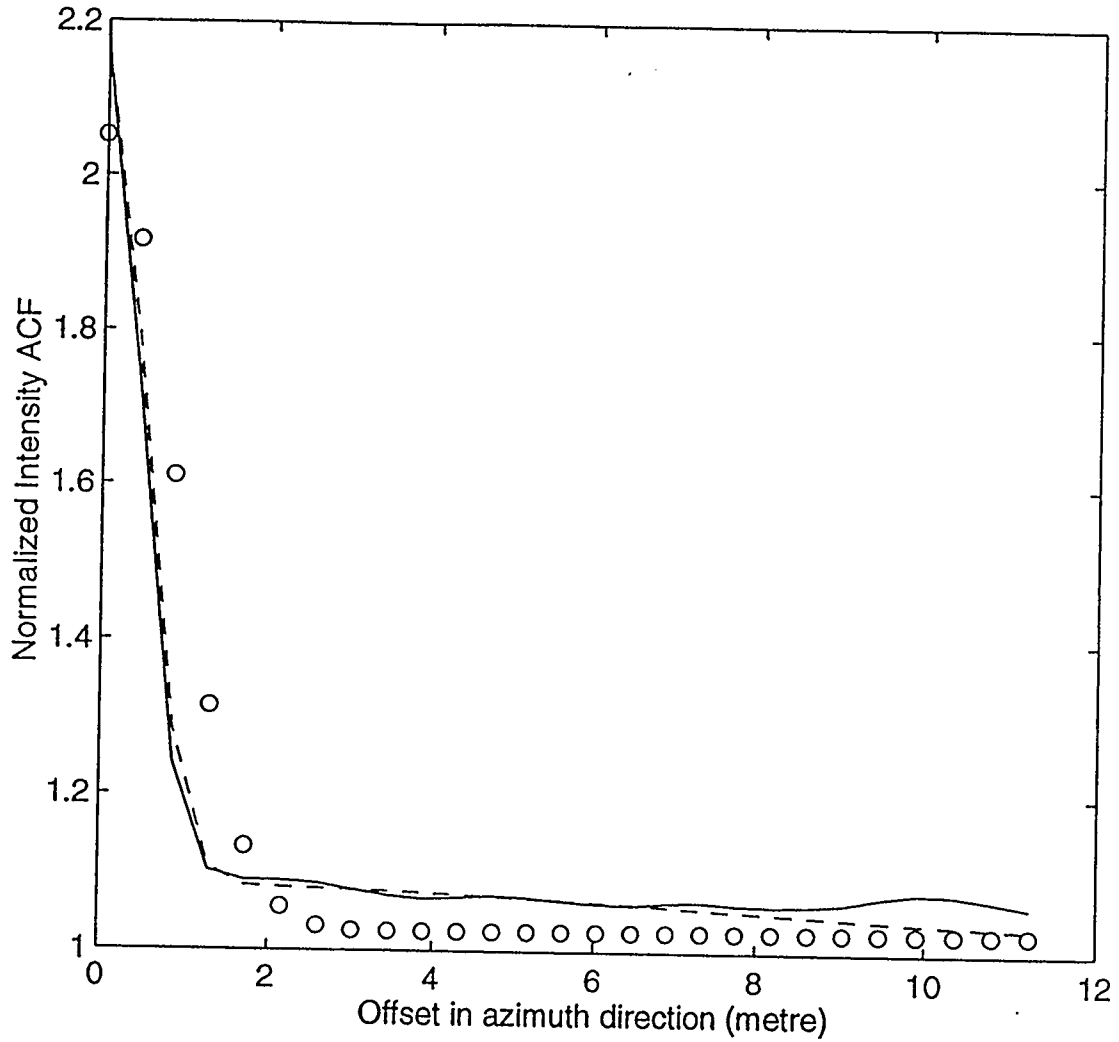


Figure 5.2 Measured and modeled ACF. Target A, Channel XHV, $n=1$, the trial focus error $\eta'=0.00$. The solid line represents the measured ACF; the dashed line represents the modeled ACF with focus error; the circles represent the ACF model not considering the focus error.

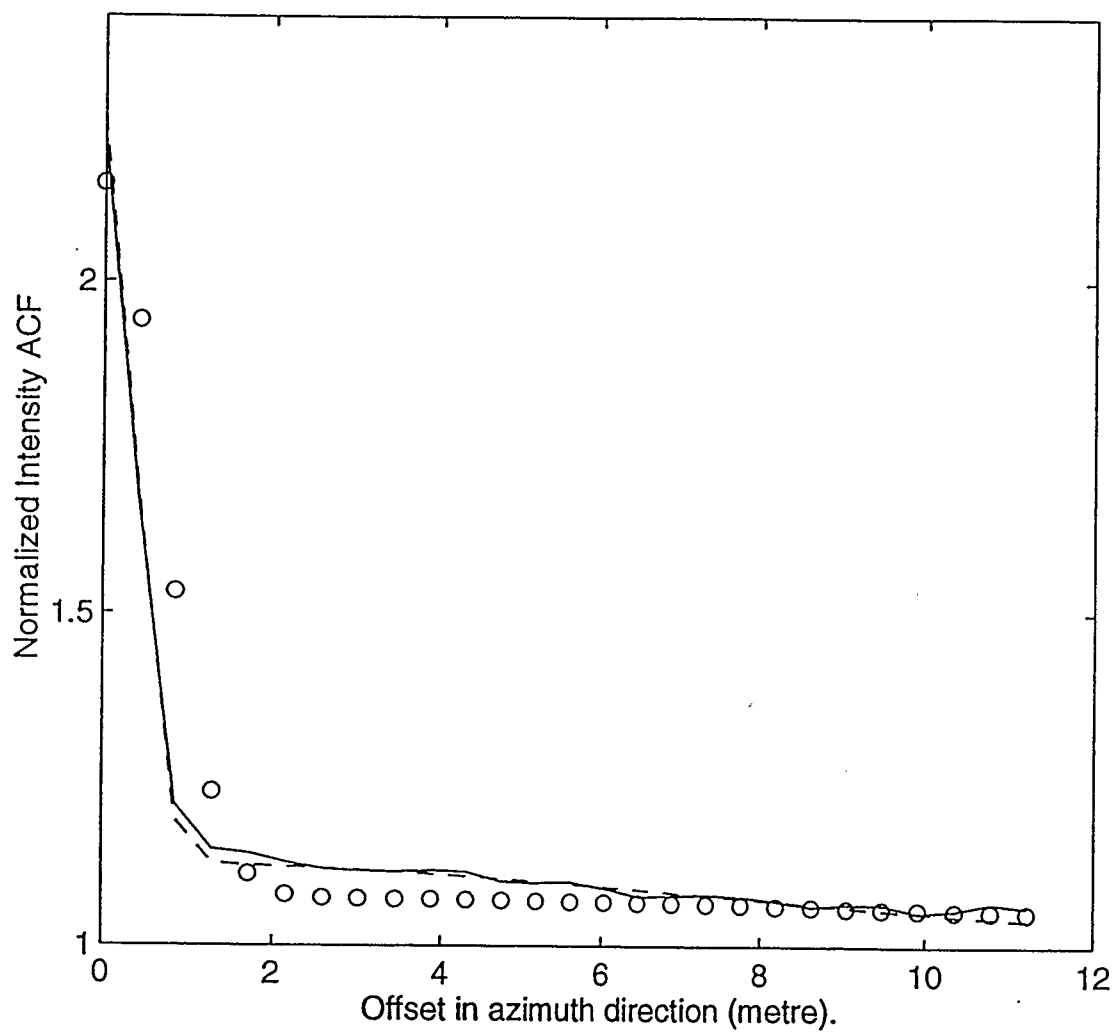


Figure 5.3 Measured and modeled ACF. Target A, Channel CHH, $n=1$, the trial focus error $\eta'=0.05$. The solid line represents the measured ACF; the dashed line represents the modeled ACF with focus error; the circles represent the ACF model not considering the focus error.

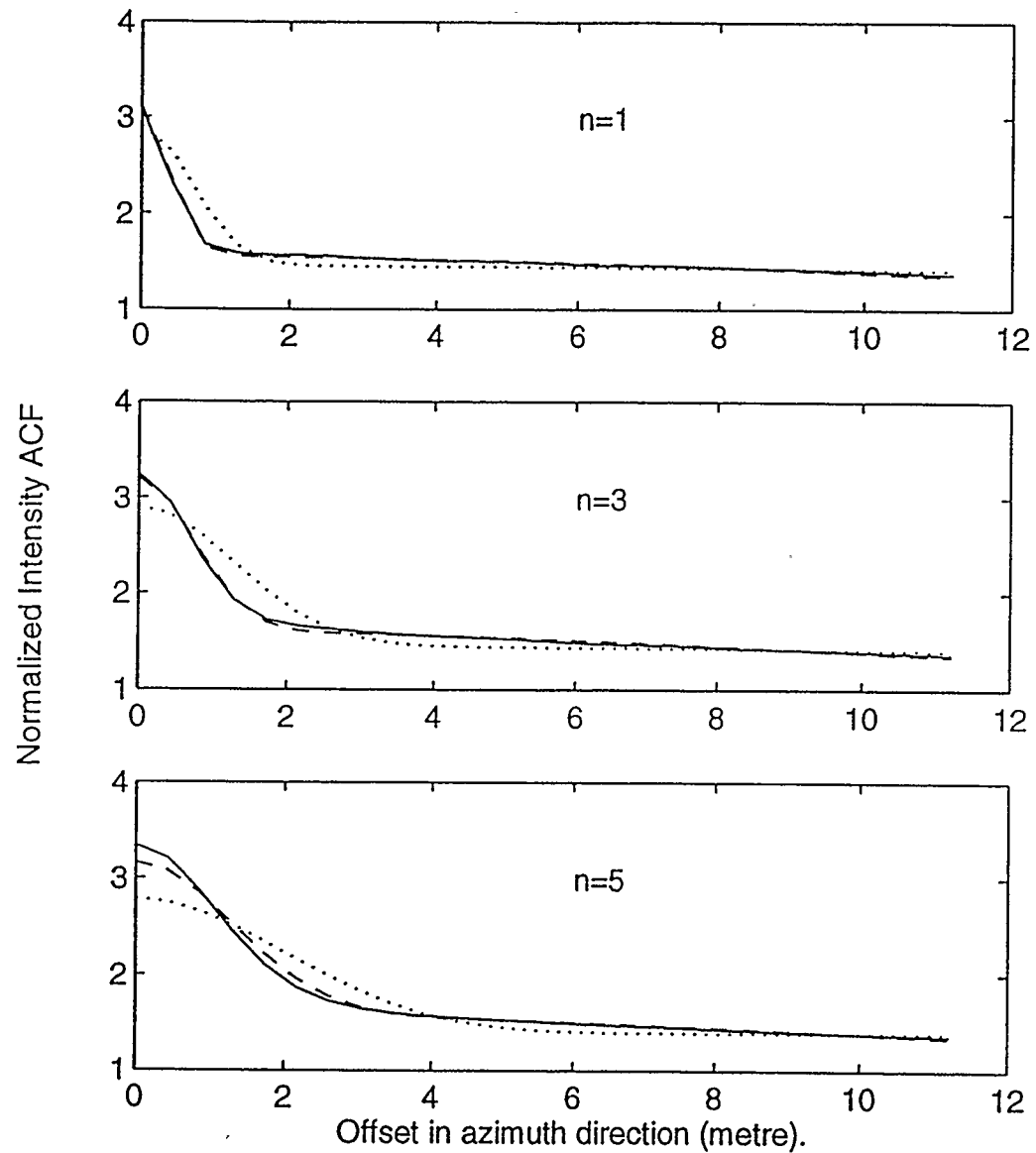


Figure 5.4 Measured and modeled ACF with different n . Target F, Channel CHH, the trial focus error $\eta'=0.03$. The solid line represents the measured ACF; the dashed line represents the modeled ACF with focus error; the dotted line represents the ACF model not considering the focus error.

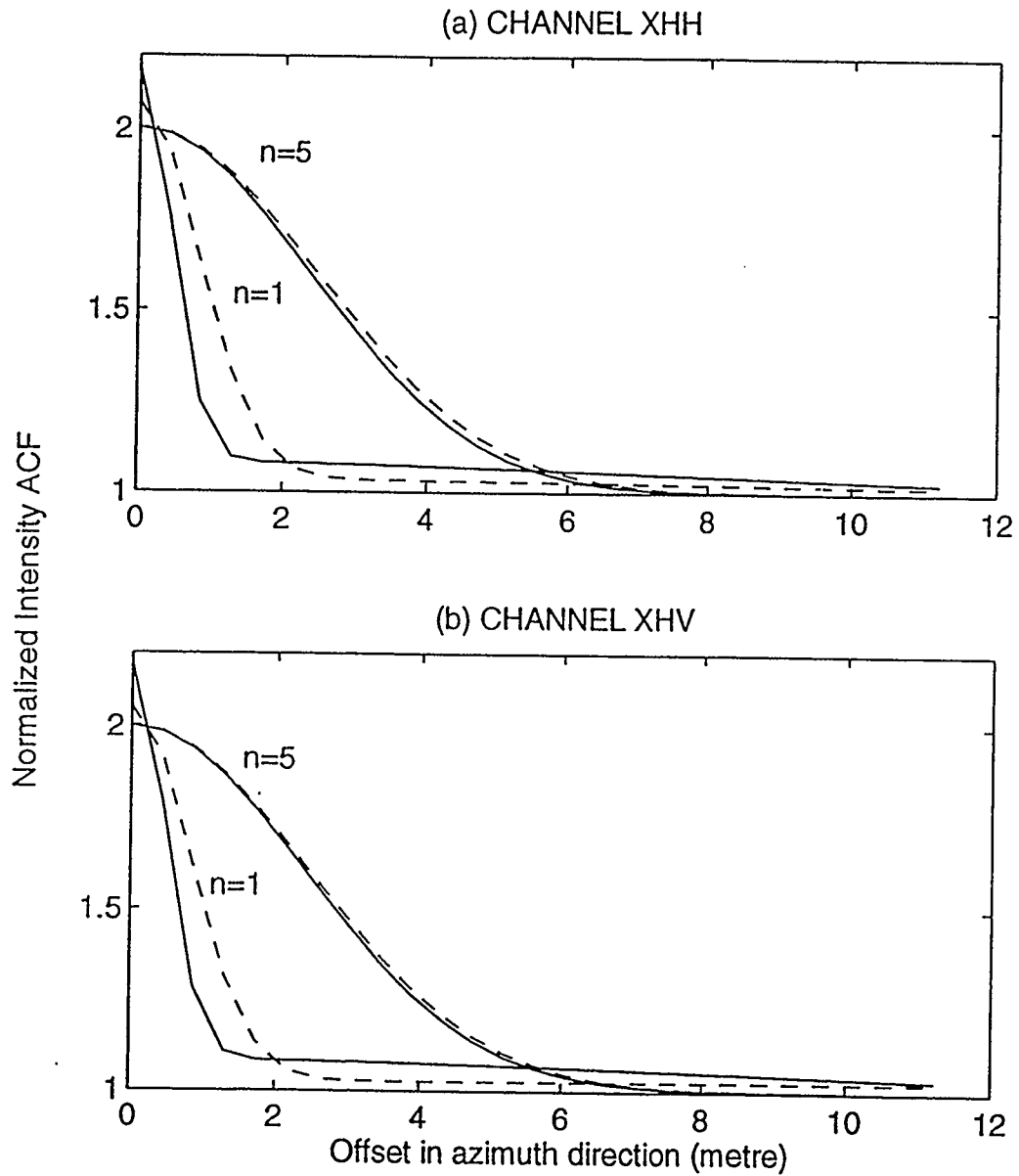


Figure 5.5 Modeled ACF of Target A of different channels, the trial focus error $\eta'=0.02$.

The solid line represents the modeled ACF with focus error; the dashed line represents the ACF model not considering the focus error.

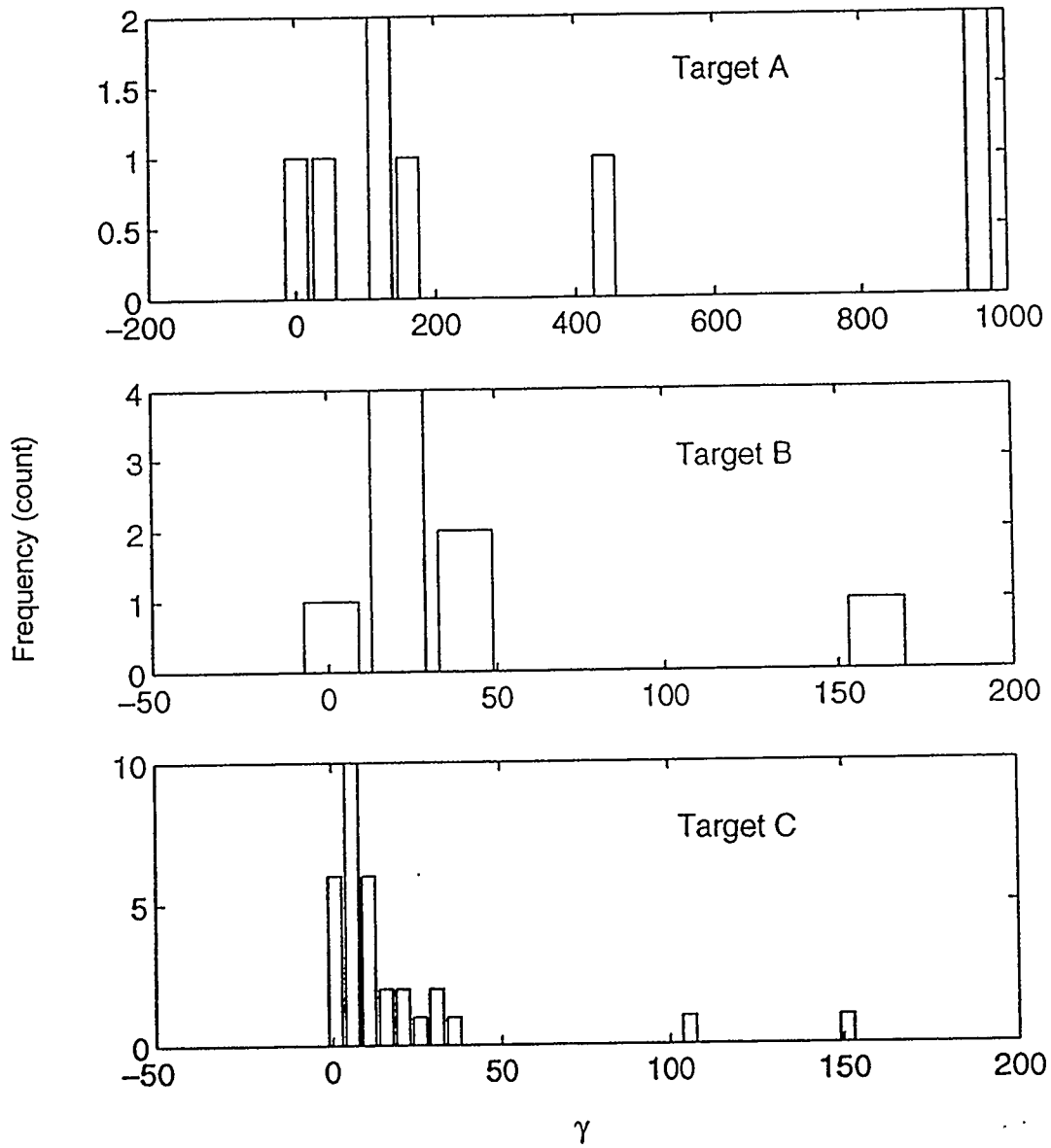


Figure 5.6 The histogram of γ of subimages (azimuth length: 128), channel XHH, $n=1$, the

trial focus error $\eta'=0.00$.

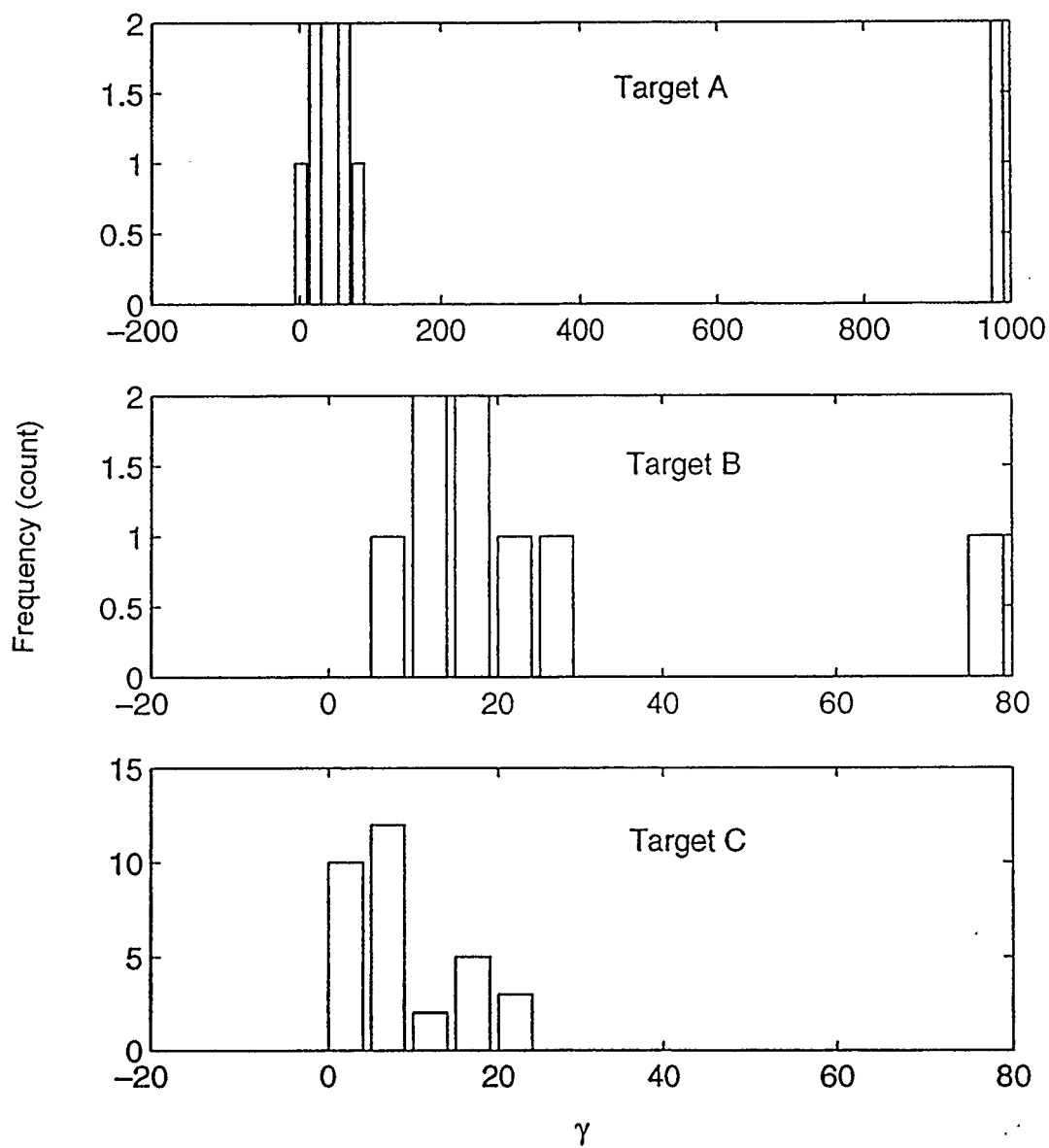


Figure 5.7 The histogram of γ of subimages (azimuth length: 128), channel CHV, $n=1$, the trial focus error $\eta'=0.00$.

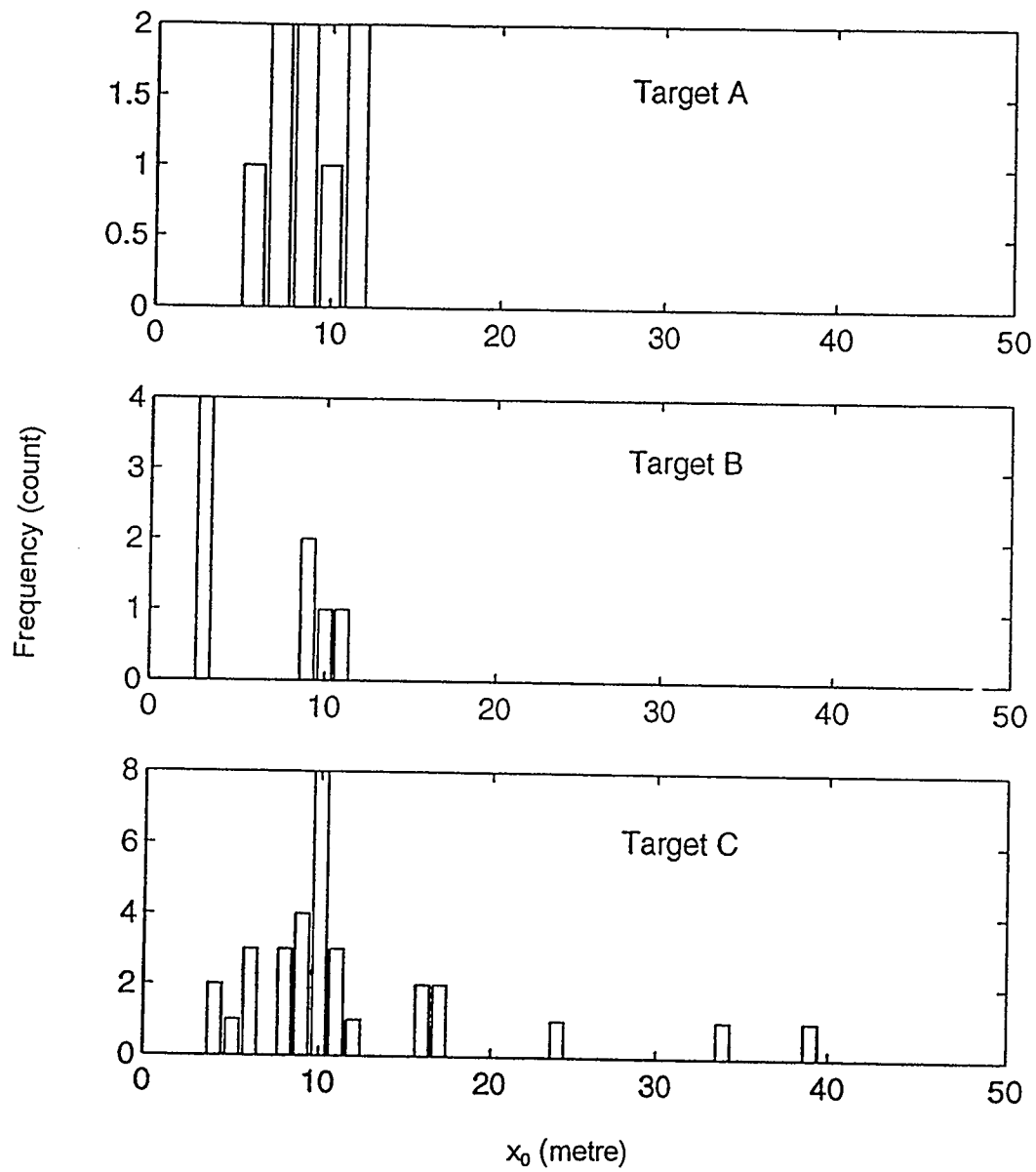


Figure 5.8 The histogram of x_0 of subimages (azimuth length: 128), channel CHH, $n=1$, the trial focus error $\eta'=0.00$.

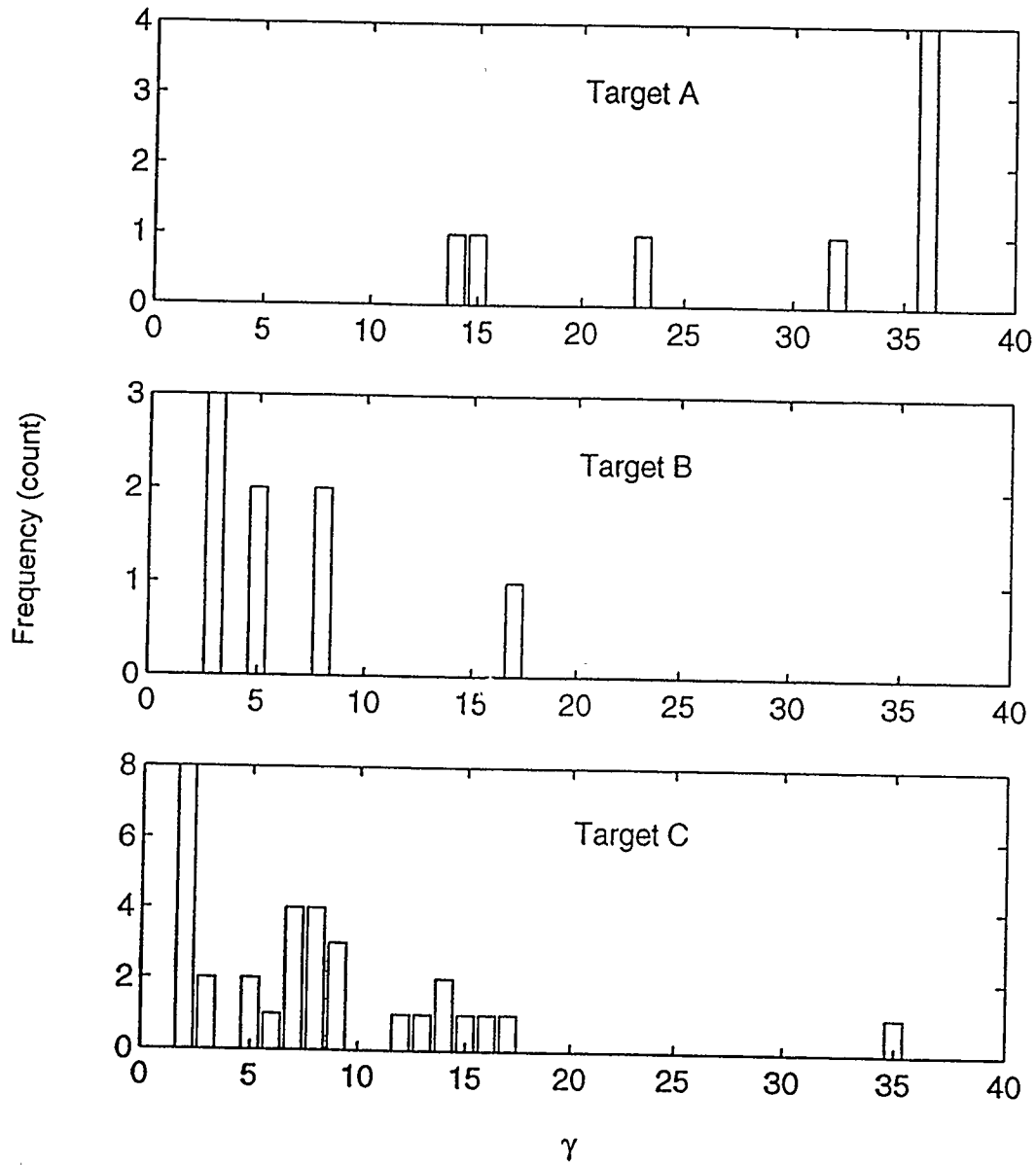


Figure 5.9 The histogram of γ of subimages (azimuth length: 128), channel CHH, $n=1$, the trial focus error $\eta'=0.00$.

CHAPTER 6

CONCLUSIONS AND RECOMMENDATIONS

6.1 Conclusions

The primary concern of this research was the extraction of information about the general SAR scene rather than specifically shaped targets. This is often described as background clutter. A K-distribution model was applied to describe the statistics of the sea ice image. The intensity ACF model was derived based on this assumption. The experiments show that the intensity ACF model including focus error is in excellent agreement with the estimated ACF of the sea ice image through the high resolution radar. The system resolution not only is a function of radar system parameters but also depends on the characteristics of the target. Generally speaking, the large look number n reduces the effect of focus error.

The theoretical and experimental fractional errors of the three targets used in the research in six channels show similarities with a few exceptions. The fractional error in the order parameter is larger than that in the correlation length. The accuracy with which the parameters of the sea ice texture can be estimated can be expressed by a modified theory. The difference between the theoretical and the experimental fractional error is a result of the edge effects introduced by the finite image size (Oliver, 1989).

The fractional error of the texture parameters is small. The three sea ice types represented by targets A, B and C can be separated by the texture parameters: order parameter and correlation length. The image size must be much larger than any

correlation length within the texture to reduce the bias in the estimation introduced by the finite size of the image. The azimuth length in the classification is 1024 and 128 pixels. Since the K-distribution model has been demonstrated to be applicable to a wide variety of natural clutter textures in coherent imagery, the results in our research suggest that texture classification based on the ACF parameter estimation is feasible. This classification algorithm is most useful for large area targets, such as sea ice, agriculture, etc. This research suggests that this new texture classification algorithm based on ACF parameter estimation of SAR image data holds promise for the discrimination between terrestrial surfaces.

6.2 Recommendations

In this research, only the one-dimensional ACF model was constructed. To better describe the texture information of the image, the texture parameters in the range direction need to be considered. A two-dimensional ACF model is essential to fully describe the image texture.

When we do the texture classification, we wish to perform this process with as small a region as possible. When the image size is reduced to 128 pixels, the texture parameters of the subimage have a normal distribution. The value ranges of the texture parameter of targets A, B and C are overlapped. The selection of an appropriate threshold is essential when classification is performed. To perform sea ice classification with smaller image size, the knowledge of the image texture is not enough. Other sources of information about the target are essential to do more accurate classification.

REFERENCES

- Argus, S. A. D. (1989). *LIMEX'89 operations plan*. Tech. rep., Canada Centre for Remote Sensing, Ottawa, CANADA.
- Barry, R. G. (1983). Arctic ocean ice and climate: perspectives on a century of polar research. *Annals of the Association of American Geographers*, 73(4), 485-501.
- Beckmann, P. and A. Spizzichino (1963). *The Scattering of Electromagnetic Waves from Rough Surfaces*. Oxford, Pergamon.
- Blacknell, D. (1994a). Comparison of parameter estimators for K-distribution. *Proceedings of the IEE*, 141(1), 45-52.
- Blacknell, D. (1994b). New method for the simulation of correlated K-distributed clutter. *Proceedings of the IEE*, 141(1), 53-58.
- Brown, W. M. (1963). *Linear Time Invariant Systems*. McGraw-Hill Book Company, New York, NY, USA.
- Carsey, F. D., S. A. Argus, M. J. Collins, B. Hilt, C. E. Livingstone and C. L. Tang. (1989). Overview of LIMEX'87 ice observations. *IEEE Transactions on Geoscience and Remote Sensing*, 27(5), 468-482.
- Cenzo, A. D. (1981). *Synthetic Aperture Radar and Digital Processing: An Introduction*. Jet Propulsion Laboratory. Report N81-18266. Pasadena, CA, USA.
- Chen, P. C. (1980). *Image Segmentation by Texture Using Estimation Technique*. Ph.D. Candidacy Dissertation, Department of Electrical Engineering and Computer Science, Princeton University.
- Collins, M. J. (1993). *RESPONSE OF AN AIRBORNE SYNTHETIC APERTURE RADAR TO SEA ICE IN THE MARGINAL ICE ZONE*, Ph.D. thesis, York University
- Conte, E., M. Longo and M. Lops (1991). Modelling and simulation of non-Rayleigh radar clutter. *IEE PROCEEDINGS-F*, 138(2), 121-130.
- Conte, E., M. D. Bisceglie, M. Lops and G. Ricci (1991). SIMULATION OF CORRELATED RANDOM FIELDS WITH GAMMA-DISTRIBUTED AMPLITUDE FOR SAR APPLICATIONS. *CH2917-0/91/0000-2397, IEEE*, 2397-2400.
- Curlander, J. C. and R. N. McDonough. (1991). *Synthetic Aperture Radar Systems and Signal Processing*. John Wiley & Son, New York, USA.

- Davis, L. S. (1975). A Survey of Edge Detection Techniques. *CGIP*, 4(3), 248-270.
- Falkingham, J. C. (1991). Operational remote sensing of sea ice. *Arctic*, 44(1), 29-37.
- Fitch, J. P. (1988). *Synthetic Aperture Radar*. Springer-Verlag, New York, USA.
- Frost, V. S. (1982). *Information Analyses and Extraction Techniques for Synthetic Aperture Radar*. Ph.D. thesis, Department of Electrical Engineering, University of Kansas.
- Galloway, M. M. (1975). Texture Analysis Using Gray Level Run Lengths. *CGIP*, 4, 172-179.
- Goodman, J. W. (1968). *Introduction to Fourier Optics*. McGraw-Hill Book Company, New York, NY, USA.
- Goodman, J. W. (1975). Statistical properties of laser speckle patterns. In Dainty, J. C. (Ed.), *Laser Speckle and Related Phenomena*. Springer-Verlag, Heidelberg, FRG.
- Gow, A. J. and W. B. Tucker III (1991). Physical and Dynamic Properties of Sea Ice in the polar Oceans. *USA Cold Regions Research and Engineering Laboratory, Monograph 91-1*.
- Herman, G. F. and W. T. Johnson. (1978). The sensitivity of the general circulation to arctic sea ice boundaries: a numerical experiment. *Monthly Weather Review*, 106, 1649-1664.
- Herman, G. F. (1986). Atmospheric modelling and air-sea-ice interaction. In Untersteiner, N. (Ed.), *The Geophysics of Sea Ice*, pp. 713-754. Plenum Press, New York, USA.
- Jackman, E. (1974). *Photon Correlation and Light Beating Spectroscopy*. Edited by H. Z. Cummins and E. R. Pike, Plenum Press, New York, NY, USA, pp. 75-149.
- Maykut, G. A. (1978). Energy exchange over young sea ice in the central arctic. *Journal of Geophysical Research*, 83, 3466-3458.
- Maykut, G. A. (1985). The ice environment. In *Sea Ice Biota* (R. A. Horner, Ed.), pp 21-82, CRC Press, Boca Raton, Florida, USA.
- Mendez, E. R. and H. M. Escamilla (1988). Contrast of speckle patterns produced by Gamma-distributed diffusers. In Morris, G. M. (Ed.), *Statistical Optics*, pp.185-192. SPIE -- The International Society for Optical Engineering, Bellingham, Washington, USA.

- McDonald, H. C. (1969). Geologic Evaluation of Radar Imagery from Darien Province, Panama. *Modern Geology*, 1, 1-63.
- Oliver, C. J. (1982). Fundamental properties of high-resolution sideways-looking radar. *IEEE PROC.*, 129(6), Pt. F., 385-402.
- Oliver, C. J. (1984). A model for non-Rayleigh scattering statistics. *OPTICA ACTA*, 31(6), 701-722.
- Oliver, C. J. (1985). Correlated K-distributed clutter models. *OPTICA ACTA*, 32(12), 1515-1547.
- Oliver, C. J. (1986). The interpretation and simulation of clutter textures in coherent images. *Inverse Problems*, 2, 481-518.
- Oliver, C. J. (1988a). The representation of correlated clutter textures in coherent images. *Inverse Problems*, 4, 843-866.
- Oliver, C. J. (1988b). Representation of radar sea clutter. *IEE PROCEEDINGS*, 135(6), pp. 497-500.
- Oliver, C. J. (1989a). The sensitivity of texture measures for correlated random clutter. *Inverse Problems*, 5, 875-901.
- Oliver, C. J. (1989b). Parameter estimation with correlated clutter textures. *Inverse Problems*, 5, 903-914.
- Oliver, C. J. (1990). Clutter classification based on a correlated noise model. *Inverse Problems*, 6, 77-89.
- Oliver, C. J. and R. G. White (1990). *RADAR CLUTTER CLASSIFICATION BASED ON NOISE MODELS AND NEURAL NETWORKS*. Controller HMSO, London.
- Oliver, C. J. (1991). Information from SAR images. *Journal of Physics D*, 24(9), 1493-1514.
- Oliver, C. J. (1993). The limits on SAR resolution imposed by autofocus uncertainty. *International Journal of Remote Sensing*, 14(3), 485-494.
- Papoulis, A. (1965). *Probability, Random Variables, and Stochastic Processes*. McGraw-Hill Book Company, New York, NY, USA.
- Palidis, T. (1977). *Structural Pattern Recognition*. Springer-Verlag.

- Posner, F. L. (1993). Texture and Speckle in High Resolution Synthetic Aperture Radar Clutter. *IEEE Transactions on Geoscience and Remote Sensing*, 31(1), 192-203.
- Press, W. H., B. P. Flannery, S. A. Teukosky and W. T. Vetterling (1992). *Numerical Recipes In C*. Cambridge University Press, New York, NY, USA.
- Pusey, P. N. (1977). *Photon Correlation Spectroscopy and Velocimetry*. Edited by H. Z. Cummins and E. R. Pike, Plenum Press, New York, NY, USA, pp. 45-141.
- Raney, R. K. and S. A. D. Argus (1988). *Science plan for LIMEX'89*. Tech. rep., Canada Centre for Remote Sensing, Ottawa, CANADA.
- Raney, R. K., S. A. D. Argus and D. Werle (Eds.) (1989). *LIMEX'89 Data Report*, Ottawa, CANADA.
- Rosenfeld, A. and J. S. Weszka (1976). *Picture Recognition and Scene Analysis*. Computer, May, 28-38
- Tsang, L., J. A. Kong and R. T. Shin (1985). *Theory of Microwave Remote Sensing*. John Wiley & Son, New York, USA.
- Ulaby, F. T., R. K. Moore and A. K. Fung (1986). Microwave Remote Sensing, Active and passive. Artech House. 3, *From Theory to Applications*, Section 21-8, 1907-1935.
- Ulaby, F. T. and M. C. Dobson (1989). *Handbook of Radar Scattering Statistics for Terrain*. Artech House, Norwood, MA, USA.
- Wadhams, P. (1986). The seasonal ice zone. In Untersteiner, N. (Ed.), *The Geophysics of Sea Ice*, pp. 825-991. Plenum Press, New York, USA.
- Ward, K. D. (1981). Compound representation of high resolution sea clutter. *Electron. Lett.*, 17, 561-563.
- Weeks, W. F. and S. F. Ackley (1982). The growth, structure and properties of sea ice. *USA Cold Regions Research and Engineering Laboratory*, Monograph 82-1.
- Whalen, A. D. (1971). *Detection of Signals in Noise*, Academic Press, New York, USA.
- Wiley, C. A. (1985). "Synthetic Aperture Radars - A paradigm for Technology Evolution." *IEEE Trans. Aerospace Elec. Sys.*, AES-21, pp. 440-443.

Zakrzewski, W. P. (1986). Sea ice conditions in the Labrador Sea - Grand Banks area. *In Proceedings of the Canadian East Coast Workshop on Sea Ice*, pp. 60-87 Bedford Institute of Oceanography, Dartmouth, Canada.